Chemical Science

ROYAL SOCIETY OF CHEMISTRY

REVIEW

View Article Online
View Journal | View Issue

Cite this: *Chem. Sci.*, 2026, **17**, 10834

Beyond static paradigms: defect dynamic evolution and advanced applications in water electrolysis

Xiaojun Wang,[a] Huilin Zhao,[a] Lei Li,*[b] Weiping Xiao,[c] Guangrui Xu,[d] Guangying Fu,*[e] Lei Wang*[a] and Zexing Wu*[a]

Received 6th March 2026
Accepted 24th April 2026

DOI: 10.1039/d6sc01899h

rsc.li/chemical-science

Electrocatalytic reactions play crucial roles in energy conversion and green chemical synthesis; however, their practical applications are often constrained by sluggish reaction kinetics, high overpotentials, and insufficient operational stability. In recent years, defect engineering has emerged as an effective structural regulation strategy, providing new opportunities to enhance electrocatalytic performance through the deliberate introduction of non-ideal structural features, such as vacancies, heteroatom dopants and interfacial architectures. Accumulating studies have demonstrated that defects not only modulate the electronic structure of catalysts and reaction pathways, but that their dynamic evolution under specific reaction conditions also exerts profound influence on the real working-state structure and long-term catalytic performance. Owing to central importance in green hydrogen production, water-splitting reactions serve as representative model systems for elucidating defect–structure–activity relationships. In this review, we systematically summarize recent advances in defect engineering for electrocatalysis, with particular focus on water electrolysis. Emphasis is placed on defect types and structural characteristics, construction strategies, dynamic evolution behaviors, and their typical applications, while current challenges and future research directions are also discussed, aiming to provide valuable guidance for the rational design and practical implementation of high-performance defect-engineered electrocatalysts.

1 Introduction

Electrocatalytic reactions play central roles in energy conversion and green chemical synthesis, with broad applications in hydrogen production, carbon dioxide conversion, nitrogen-cycle reactions, and electrochemical energy storage systems.[1–3] Compared with conventional thermocatalytic processes, electrocatalysis relies on externally applied electric fields to drive electron-transfer reactions, offering advantages such as mild operating conditions, high energy utilization efficiency, and strong process tunability.[4] However, most key electrocatalytic reactions intrinsically involve complex multi-electron transfer processes and coupled reaction intermediates, leading to sluggish reaction kinetics, high overpotentials, and insufficient operational stability. These issues continue to severely limit the further development of electrocatalytic technologies.[5,6] Consequently, achieving fundamental understanding and rational regulation of structure–activity relationships from the materials-structure perspective has emerged as one of the central scientific challenges in contemporary electrocatalysis.

The electronic structure of catalysts, their local coordination environments, and interfacial reaction properties are widely recognized as decisive factors governing electrocatalytic activity and selectivity.[7] Conventional catalysts based on ideal crystalline structures often struggle to simultaneously optimize active-site exposure, charge-transfer efficiency, and structural stability, which has prompted increasing research interest in non-ideal structural systems. As ubiquitous non-periodic features in crystalline materials, defects can effectively break local symmetry and electronic neutrality, generating low-coordination, highly reactive catalytic sites on surfaces or interfaces, while markedly modulating the electronic states and interfacial reaction behavior of catalysts.[8]

In recent years, defect engineering has emerged as a key strategy for electrocatalytic material design. By introducing vacancy defects, heteroatom dopants, grain boundaries (GBs),

---

[a] *State Key Laboratory of Advanced Optical Polymer and Manufacturing Technology, Key Laboratory of Eco-chemical Engineering, Ministry of Education, International Science and Technology Cooperation Base of Eco-chemical Engineering and Green Manufacturing, College of Chemistry and Molecular Engineering, Qingdao University of Science & Technology, 53 Zhengzhou Road, Qingdao, 266042, P. R. China. E-mail: splswzx@qust.edu.cn; inorchemwl@126.com*

[b] *College of Biological, Chemical Sciences and Engineering, Jiaxing University, Jiaxing, Zhejiang 314001, China. E-mail: leili@mail.zjxu.edu.cn*

[c] *College of Science, Nanjing Forestry University, Nanjing, 210037, P. R. China*

[d] *College of Materials Science and Engineering, Qingdao University of Science & Technology, 53 Zhengzhou Road, Qingdao, 266042, P. R. China*

[e] *Key Laboratory of Photoelectric Conversion and Utilization of Solar Energy, Qingdao Institute of Bioenergy and Bioprocess Technology, Chinese Academy of Sciences, CN-266101 Qingdao, China. E-mail: fugy@qibebt.ac.cn*

and heterointerfaces, the electronic structure and catalytic performance can be precisely regulated across different spatial scales.[9] For example, Arandiyan *et al.* systematically investigated the effect of oxygen vacancies (V_O) on the oxygen evolution reaction (OER) performance using $LaNiO_3$ with abundant V_O and vacancy-free $LaNiO_3$ as model systems, revealing the crucial role of defects in enhancing electrical conductivity, modulating the electronic structure, and improving catalytic activity.[10] In addition, $CeO_{2-x}/MoO_{3-x}/RuO_2$ heterointerface defect systems were employed to further elucidate the influence of different defect configurations on the hydrogen evolution reaction (HER) and catalytic ozonation performance.[11] Moreover, defect engineering strategies have also been extended to the nitrate reduction reaction, highlighting their broad applicability across diverse electrocatalytic processes.[12] Overall, defect-engineered catalysts often exhibit superior performance compared with their ideal crystalline counterparts across wide ranges of electrocatalytic reactions.[13]

Notably, defects are no longer regarded as static structural features with the continued advancement of research. Increasing evidence from *in situ* and *operando* characterization studies indicates that defects undergo continuous generation, migration, aggregation, and reconstruction during material synthesis and practical electrocatalytic operation. Such dynamic evolution processes largely determine the true working-state structure of catalysts and their long-term performance.[14] Consequently, structure–activity relationships established solely on the basis of static characterization exhibit inherent limitations, and reassessing the role of defects in electrocatalysis from dynamic perspectives has emerged as an important research direction.

Among various electrocatalytic reaction systems, water electrolysis occupies a particularly prominent status due to critical roles in green hydrogen production and renewable energy conversion.[15] Along with its well-defined reaction pathways and significant industrial relevance, it serves as an ideal model system for elucidating the dynamic evolution mechanisms of defects and their structure–activity relationships.[16,17] In the context of the HER and OER, defect engineering has demonstrated pronounced advantages in enhancing catalytic activity, regulating reaction pathways, and improving structural stability, thereby providing representative model systems for elucidating the intrinsic relationships among defects, structure, and catalytic performance.[18]

Based on this background, this review systematically surveys and critically analyzes recent progress in defect engineering for electrocatalytic systems, with particular focus on roles in structural regulation and structure–activity relationships. Emphasis is placed on defect types and structural characteristics, construction strategies, dynamic evolution behavior, and representative applications in water electrolysis (Scheme 1), with the aim of serving as comprehensive guidance for rational design and practical implementation of defect-engineered electrocatalysts.

2 Classification of defects and structure–activity relationships

Defects generally refer to localized disordered states in crystalline materials that deviate from ideal periodic lattice arrangements, including the absence, displacement, and substitution of atoms or ions, as well as the incorporation of heteroatoms. The introduction of defects disrupts local charge neutrality and lattice symmetry, inducing charge redistribution and generating non-ideal coordination sites with distinct chemical reactivity. From a structure–property perspective, deliberately engineered defects with tailored types and spatial distributions can effectively modulate the electronic density of states, surface energy, and adsorption behavior of reaction intermediates.[19,20] These modifications in turn govern the catalytic reaction energetics and kinetics, enabling the synergistic optimization of catalytic activity and stability.[21,22]

2.1 Types of defects

From the perspective of structural scale and spatial extension, crystal defects can generally be classified into point defects, line defects, planar defects, and bulk defects (Fig. 1 illustrates

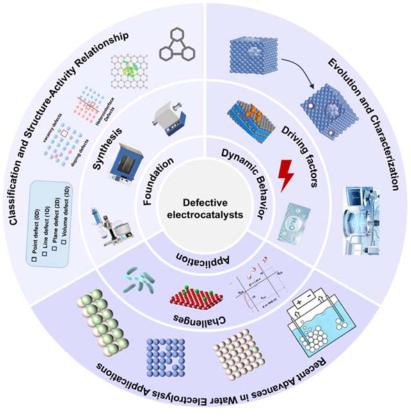

Scheme 1 Systematic overview of defect engineering for electrocatalysis.

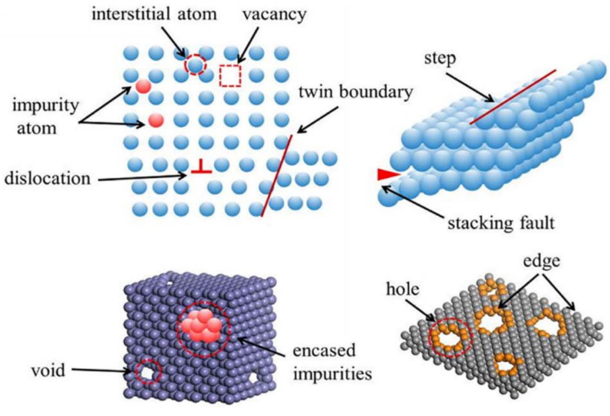

Fig. 1 Schematic illustrating various defects and their respective features in crystals with multiple dimensions.[33] Copyright 2020 Elsevier B.V.

various defects and their corresponding features in multidimensional crystals). This classification framework provides a fundamental basis for understanding defect characteristics and their structure–activity relationships. Point defects refer to localized lattice imperfections at the atomic scale (approximately 0.1–1 nm), involving the absence, displacement, or additional introduction of single atoms or a small number of atoms. They represent the most common type of defects. Typical point defects include vacancies and interstitial defects. Vacancy defects arise when atoms or ions that should occupy lattice sites in an ideal crystal are missing. Among them, V_O are particularly representative, as they can significantly alter local charge distribution and coordination environments, exposing more low-coordinated and highly reactive sites on catalyst surfaces. This effect facilitates the adsorption and transformation of key reaction intermediates, reducing reaction energy barriers and overpotentials.[23,24] In contrast, interstitial defects are formed when relatively small atoms or ions occupy interstitial sites within the lattice. Such defects can induce local lattice expansion or distortion, regulate interlayer spacing, and improve electronic transport properties, while simultaneously increasing the accessibility of active sites and enhancing overall electrocatalytic performance.[25] Line defects are typically represented by dislocations. The presence of dislocations leads to continuous lattice distortion, causing atoms in the vicinity of the dislocation core to adopt high-energy and asymmetrically coordinated configurations, which can act as potential highly active reaction sites. Moreover, dislocations are often accompanied by pronounced local strain fields. These strain effects can effectively modulate the electronic structure of metal centers and optimize the adsorption energies of reaction intermediates (such as *OH and *O), thereby accelerating electrocatalytic reaction kinetics.[26,27]

Surface defects mainly include GBs and stacking faults. GBs are interfacial regions between crystallites with different orientations, characterized by highly disordered atomic arrangements, abundant dangling bonds, and elevated interfacial energies, making them intrinsically active regions for electrocatalytic reactions. In electrocatalytic systems, the introduction of GBs is often associated with an increased concentration of vacancy defects (*e.g.*, V_O), which enhances electron transport and markedly improves catalytic activity.[28] In addition, stacking faults refer to deviations from the ideal periodic stacking sequence of atomic layers in crystals. Such faults disrupt the inherent stacking symmetry and can stabilize associated dislocations, leading to localized lattice distortion regions. These regions are typically enriched with twin boundaries, steps, and corner atomic configurations, which introduce strain effects and strongly modulate the electronic structure of the material, ultimately influencing its electrocatalytic performance.[29,30] Bulk defects are three-dimensionally distributed imperfections that deviate from ideal crystal periodicity, with characteristic sizes ranging from the atomic scale to micrometers or even larger. They are predominantly located within the interior of materials rather than being confined to surfaces or interfaces. Cavities represent representative forms of bulk defects. The internal space and edge regions of cavities can provide large numbers of exposed low-coordination active sites, while also facilitating adsorption, mass transport, and rapid release of reaction intermediates and gaseous products. These features promote sustained catalytic reactions and contribute to improved long-term stability of the electrocatalytic system.[31,32] In the following sections, we will systematically review three representative types of defects and discuss in detail their structure–activity relationships as well as the underlying mechanisms in electrocatalytic processes.

2.1.1 Vacancy defects.

Vacancy defects are among the most common intrinsic defects in materials and typically originate from structural imperfections or non-stoichiometric compositions, without the introduction of foreign impurity atoms. According to the type of missing species, vacancy defects can be further classified into cation vacancies, anion vacancies, and cation–anion composite vacancies.

In recent years, anion vacancies-such as oxygen, sulfur, selenium, and phosphorus vacancies-have been extensively investigated in electrocatalysis and proven to be effective for tuning catalytic performance.[34,35] Among them, V_O are the most representative anion vacancies in metal oxides. Their formation directly modifies the local coordination environment of metal centers and is often accompanied by localized electron trapping and redistribution. Consequently, defect states are introduced near the band edges, leading to bandgap narrowing or enhanced effective electrical conductivity, facilitating electron transport and interfacial charge-transfer kinetics.[36] Extensive

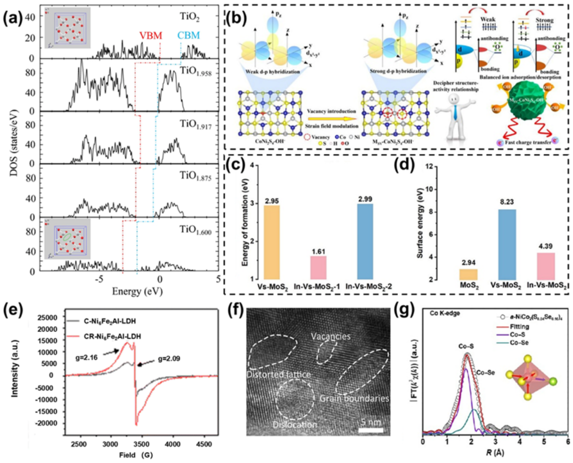

Fig. 2 (a) Total density of states (TDOS) of TiO_2 and TiO_{2-x} near the Fermi level.[36] Copyright 2023 Springer Nature. (b) Theoretical models of $CoNi_2S_4–OH^-$ and M_{SV}-$CoNi_2S_4–OH^-$ and schematic illustration for their various d–p orbital hybridization states induced by the V_S-modulated strain field and the corresponding material feature.[39] Copyright 2025 Wiley-VCH. (c) Energy of formation of V_S-MoS_2, In-V_S-MoS_2-1, and In-V_S-MoS_2-2.[41] Copyright 2025 Wiley-VCH. (d) Surface energy of MoS_2, V_S-MoS_2, and In-V_S-MoS_2.[41] Copyright 2025 Wiley-VCH. (e) Electron paramagnetic resonance (EPR) spectra of C-Ni_6Fe_2Al-LDH and CR-Ni_6Fe_2Al-LDH.[45] Copyright 2024 Royal Society of Chemistry. (f) High-resolution transmission electron microscopy (HRTEM) image of P_x-$CoMoO_{4-x}$/NF.[50] Copyright 2023 Wiley-VCH. (g) X-ray absorption spectroscopy (XAS) fitting in *R* space at the Co K-edge of a-$NiCo_2(S_{0.84}Se_{0.16})_4$.[52] Copyright 2025 Tsinghua University Press.

experimental and theoretical studies demonstrated that the introduction of V_O in TiO_2 induced bandgap narrowing and localized electronic states (Fig. 2a). These electronic structure modulations facilitate charge transport and optimize reaction-related electronic processes, thereby establishing a clear structure–property relationship between defect configuration and catalytic performance.[37] For metal sulfides, intrinsically low electrical conductivity and sluggish interfacial charge-transfer kinetics severely limit their practical electrocatalytic applications. To address these challenges, the introduction of sulfur vacancies (V_S) has been recognized as an effective regulation strategy.[38] Researchers[39] proposed V_S-induced local strain strategies to enhance d–p orbital hybridization. The concentrated tensile strain introduced by V_S significantly lowered the Co d-orbital energy levels and shifted the d-band center upward, strengthening Co-3$d_{x^2-y^2}$/O-2p_z orbital hybridization and facilitating charge transfer and accelerated redox kinetics, underscoring the strong coupling between defect-induced structural distortion and catalytic performance (Fig. 2b). However, it should be noted that V_S often impart high lattice distortion energies and complex atomic rearrangements to metal sulfides. Moreover, their elevated surface energies may lead to structural instability during long-term cycling, ultimately resulting in performance degradation.[40] To overcome the insufficient stability associated with V_S, Hui *et al.*[41] introduced In atoms into V_S-MoS_2 to construct an In-V_S-MoS_2 system. It was found that the formation energy of V_S near In sites (1.61 eV) was substantially lower than that near Mo sites (2.99 eV, Fig. 2c). Meanwhile, the surface energy of pristine MoS_2 was 2.94 eV, which increased to 8.23 eV after V_S formation, whereas In doping reduced it to 4.39 eV (Fig. 2d). These results further reveal the role of dopants in regulating defect energetics and stabilizing the catalyst framework.

Similar to anion vacancies, the construction of cation vacancies is also an important strategy for enhancing intrinsic catalytic activity, with comparable mechanisms for regulating electronic structures and reaction kinetics. Notably, cation vacancies generally exhibit higher structural stability under electrocatalytic conditions than anion vacancies.[42] However, owing to the relatively large atomic mass of metal cations, high migration barriers, and strong metal–anion bonding, the removal of metal cations from lattices is thermodynamically and kinetically unfavorable, making the construction of high-purity single cation vacancies under mild conditions highly challenging. To address this limitation, sacrificial dopants have been introduced as universal strategies for generating cation vacancies.[43] Wang *et al.*[44] selectively leached Zn *via* electrochemical reconstruction to successfully fabricate Zn-vacancy-modified NiFeOOH. The introduction of Zn vacancies stabilized Fe sites as "hydroxyl (OH) pumps", enhancing local OH adsorption and accelerating V_O refilling through atomically unhindered spillover pathways. In addition, Zn vacancies optimized the O 2p band center and strengthened metal–oxygen (M–O) covalency, activating lattice oxygen (O_L) participation in the reaction. This work clearly linked vacancy-induced electronic and geometric modifications with enhanced OER kinetics and structural robustness under lattice oxygen mechanism (LOM) operation. Beyond single vacancies, cation–anion composite vacancies can integrate multiple vacancy effects to synergistically optimize reaction pathways. Researchers[45] selectively removed Al from NiFeAl-LDH *via* alkaline etching to generate cation vacancies, followed by electrochemical redox treatment to introduce V_O, successfully constructing composite vacancies. EPR measurements confirmed the presence of such composite defects (Fig. 2e). Electrochemical evaluations demonstrated that these composite vacancies not only enhanced electrical conductivity, charge-transfer capability, and ion transport rates but also reduced the activation energy barrier for the OER, providing valuable insights for constructing uniformly distributed cation–anion composite vacancy defects.

2.1.2 Doping-induced defects. Heteroatom doping is one of the most common and effective point-defect engineering strategies. Essentially, introduction of foreign atoms into host lattices through substitutional or interstitial incorporation disrupts intrinsic periodicity, structural integrity and stoichiometry of crystals, resulting in lattice defects collectively referred to as doping defects. Due to differences in the ionic radius, valence states, and coordination tendency between dopants and host atoms, doping typically induces lattice strain, leading to distortions in bond lengths and angles.[46] Notably, valence-mismatched doping necessitates the maintenance of overall charge neutrality through charge-compensation mechanisms inherent to defect chemistry. Specifically, when lower-valence dopants substitute higher-valence metal sites (p-type doping), charge compensation is typically achieved by generating anion vacancies (*e.g.*, V_O) or holes. Conversely, when higher-valence dopants replace lower-valence metal sites (n-type doping), charge balance can be restored *via* electron compensation or the formation of cation vacancies.[47] According to the chemical nature of dopants, doping strategies are generally classified into non-metal doping, metal doping and co-doping.

Non-metal elements, such as C, N, P, and S, are commonly used dopants in electrocatalytic materials. Their incorporation can effectively tune electronic structures,[48,49] create additional active sites, and lower reaction kinetic barriers. Qi *et al.*[50] synthesized a series of P-doped $CoMoO_4$ nanowires. HRTEM and X-ray photoelectron spectroscopy (XPS) analyses identified high densities of lattice defects induced by P doping, including vacancies, dislocations and lattice distortions (Fig. 2f), which increased the density of unsaturated active sites and significantly modulated the electronic structure of the active metal centers. The formation of these defects was mainly attributed to charge imbalance caused by partial substitution of $MoO_4{}^{2-}$ groups with $PO_4{}^{3-}$, as well as structural distortions induced by differences in the atomic radius. These results indicate that P-doping-driven defect engineering plays a decisive role in tuning the structure–electronic property relationship of $CoMoO_4$. Compared with S and P doping, Se exhibits a broader oxidation-state range and more stable intermediate valence states, endowing it with unique advantages in electronic structure regulation.[51] Researchers[52] reported that Se-doped $NiCo_2S_4$ samples with different Se contents all exhibited amorphous characteristics, highlighting that defect-rich amorphous phases could be effectively engineered *via* heteroatom doping. Owing to the larger atomic radius of Se, lattice strain and mismatch were introduced, promoting strain relaxation in $NiCo_2S_4$ hollow nanorods and inducing localized structural dissociation and pore formation. XAS further confirmed that Se incorporation significantly increased the electronic density around Co centers and induced severe local lattice distortion (Fig. 2g), indicating enhanced metal–ligand bond flexibility in the amorphous framework and ultimately reducing the OER rate-determining step (RDS) energy barrier from 4.11 eV to 2.81 eV and markedly accelerating reaction kinetics. In addition to non-metal dopants, metal doping has also been widely employed to construct efficient electrocatalysts. Zhang *et al.*[53] successfully fabricated an interstitial Mn-doped $NiFeSe_2$ ($Ni_{0.8}Fe_{0.2}Mn_{0.1}Se_2$) self-supported anode. Mn doping enhanced the electronic structure of $NiFeSe_2$ through orbital hybridization and interstitial $[MnSe_4]$ tetrahedral formation, which elevated the Fermi level and narrowed the bandgap. These electronic structure modulations governed charge transport properties and were responsible for the accelerated charge-transfer kinetics.

2.1.3 Heterointerface defects. Heterointerface defects represent another frequently encountered and highly tunable class of defects in defect engineering. They typically form at the contact interfaces between two or more materials with different crystal phases, chemical compositions or electronic structures. Fundamentally, these defects arise from pronounced differences in lattice constants, crystal symmetry, bonding characteristics, and Fermi levels across the interface. The combined effects of these disparities lead to lattice distortion and bond cleavage, resulting in the formation of dangling bonds and coordinatively unsaturated sites, thus forming bulk and interfacial defects. Specifically, lattice-parameter mismatch is often accommodated by the introduction of dislocations or lattice distortions at the interface. Meanwhile, abrupt changes in local chemical environments can trigger vacancy formation or localized dopant enrichment, while phase disparities between crystalline–amorphous interfaces or different polymorphs further promote the formation of disordered interfacial regions. Wu *et al.*[54] constructed a $Ni_{0.85}Se/WO_{2.90}$ heterojunction catalyst and employed HRTEM to confirm the presence of the heterointerface. Lattice defects and distortions originating from V_O were observed by HRTEM, which were beneficial for optimizing the behavior of reaction intermediates. Interfacial lattice distortions modified Ni–Ni interatomic distances, while vacancy formation lowered the oxidation state of W and weakened W–O bond strength, as evidenced by XAS analysis. These results collectively established a clear structure–property relationship, in which interfacial defect-induced structural reconstruction and electronic modulation synergistically regulate intermediate adsorption energetics, thereby lowering the Gibbs free energy barrier of the RDS. In addition, lattice regulation and strain effects at heterogeneous interfaces have also been fully verified in other systems, further supporting the universality of this strategy. Fu *et al.*[55] synthesized Os/OsP_2 heterojunctions *via* the quasi-solid-state microwave method. Geometric phase analysis (GPA) revealed pronounced interfacial strain effects, which facilitated the exposure of more active sites and resulted in excellent HER performance.

Overall, vacancy defects can significantly enhance the intrinsic catalytic activity by introducing unsaturated coordination sites and modulating the electronic structure. However, owing to their high surface energy, they often suffer from limited structural stability during long-term operation. In contrast, doping-induced defects offer a more controllable strategy for tuning the electronic structure and defect energetics, which not only improves electrical conductivity but also stabilizes the catalyst framework; nevertheless, their effectiveness in enhancing catalytic activity strongly depends on the nature and physicochemical properties of the dopants. Heterointerface defects, arising from lattice mismatch and electronic coupling between different phases, enable synergistic regulation of charge distribution and adsorption energetics, thereby allowing simultaneous improvement in catalytic activity and structural stability to a certain extent. Clarifying the functional roles of different defect types provides important guidance for the rational design of defect-engineered catalysts.

3 Synthesis methods

The rational selection and optimized combination of synthetic strategies are the technical foundation for the precise construction and controllable regulation of defects, and the characteristics of different methods in defect control are systematically summarized as follows.

3.1 Chemical approaches

Chemical treatments represent one of the most commonly employed and effective strategies for constructing defect-rich electrocatalysts. Compared with physical methods, chemical approaches are generally conducted under relatively mild conditions. The generation of defects is jointly governed by thermodynamic equilibrium and reaction kinetics, which affords greater tunability but with relatively limited defect concentration.[56] Various defect structures favorable for electrocatalytic performance, including vacancies, heteroatom substitutions and localized structural reconstructions, are achievable through the rational design of reaction environments and tailored chemical treatment pathways.

3.1.1 Hydrothermal/solvothermal methods. Hydrothermal/solvothermal methods offer highly controllable strategies in the defect engineering of electrocatalysts. Fundamental principles underlying these methods involve regulation of crystal growth kinetics in high-temperature and high-pressure liquid-phase environments, thereby promoting formation of abundant defect structures. Rational tuning of reaction temperature, time scale, precursor concentration and chemical modifiers drives lattice anion dissociation and external atom incorporation into crystallographic sites, giving rise to abundant point defects, particularly V_O.[57–59] For example, Yang *et al.*[60] developed the graphene aerogel (GA)-supported nickel–cobalt oxide (Ni–Co oxide, GA/NCO-*x*) nanowire catalyst *via* a combined hydrothermal and pyrolysis strategy. Precise control over the hydrothermal reaction

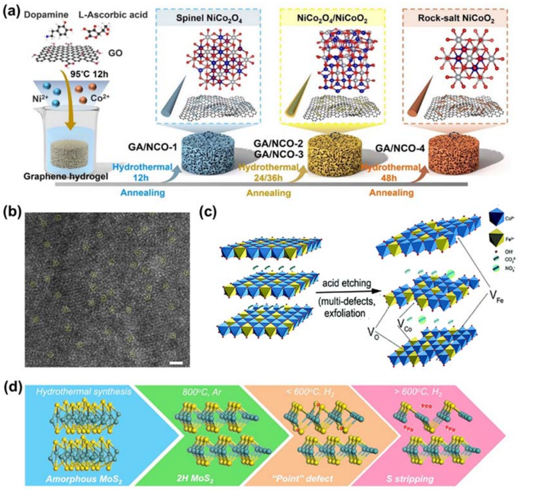

Fig. 3 (a) Illustration of the synthetic procedure of GA/NCO-2 and the effect of reaction duration on the structure.[60] Copyright 2024 Wiley-VCH. (b) Aberration-corrected transmission electron microscopy (AC-TEM) image of Ru_1/D-NiFe LDH (isolated Ru atoms are marked with yellow circles).[66] Copyright 2021 Springer Nature. (c) E-CoFe LDHs after HNO_3 etching.[67] Copyright 2017 Royal Society of Chemistry. (d) Evolution of the different structures of MoS_2.[68] Copyright 2019 American Chemical Society.

time enabled accurate regulation of V_O concentration, which in turn induced topological phase transition from the spinel phase ($NiCo_2O_4$) to the rock-salt phase ($NiCoO_2$) (Fig. 3a). First, V_O concentration functioned as a switch to modulate the extent of phase transition: high concentrations accumulated during extended hydrothermal treatment drove the deep diffusion of V_O from the surface to the bulk along the concentration gradient. Second, V_O acted as a trigger for lattice rearrangement: to counteract the charge imbalance induced by V_O, tetrahedrally coordinated Co^{3+} was reduced *in situ* and migrated to octahedral interstitial sites, initiating atomic rearrangement of the spinel structure. This V_O-mediated ion migration effectively reduced the energy barrier for rock-salt phase formation, allowing Ni and Co ions to fully occupy all octahedral sites in the rock-salt structure and accomplish the phase transition.

3.1.2 Chemical etching methods. Chemical etching is an efficient approach for introducing defect engineering into transition-metal-based electrocatalysts. Its core principle lies in the selective dissolution or etching of specific components from the catalyst surface or lattice, enabling precise control over defect type, density, and spatial distribution, and thus optimizing electronic structures and catalytic kinetics.[61,62] Among various etching strategies, acid and alkaline etching are widely used to construct abundant active sites or introduce atomic-scale defects.[63,64] Through the selective leaching of soluble components, alkaline etching can directionally generate stable cation vacancies,[65] which act as intrinsic riveting sites to effectively anchor single atoms, forming a typical cation-vacancy-riveting-effect-based strategy for the construction of single-atom catalysts (SACs). Hou *et al.*[66] generated M^{3+} cation vacancies in layered double hydroxides (LDHs) *via* alkaline etching. These vacancies served as robust anchoring sites, enabling the highly dispersed immobilization of Ru single atoms (Fig. 3b) on the LDH surface while effectively suppressing aggregation. The above phenomenon was further confirmed by AC-TEM. The synergistic effect between cation vacancies and single atoms facilitated charge transfer and increased the accessible active site density, thereby accelerating water-splitting kinetics and enhancing the intrinsic HER and OER activities. It should be noted that acid etching required more stringent control over reaction conditions and reagent dosage compared with alkaline etching. Excessive acid can severely damage the structural framework of materials, potentially leading to complete collapse.[31] Zhou *et al.*[67] employed HNO_3 to etch cobalt–iron hydroxides and successfully prepared ultrathin E-CoFe-LDH (Fig. 3c). According to X-ray diffraction (XRD) and TEM analyses, moderate acid etching retained the layered architecture of the catalyst while introducing cavity defects within the nanosheets. Further increasing the acid dosage to 3 mL led to severe structural failure and complete collapse. Further XAS and TEM analyses confirmed the simultaneous induction of multiple vacancy defect types by acid etching. Density functional theory (DFT) calculations demonstrated that metal vacancies (V_M) reduced the adsorption energy of water molecules, thereby facilitating reactant activation, whereas V_O enhanced the conductivity of OER intermediates and optimized their adsorption energies by modulating the electronic structure. The synergistic interplay between these vacancies markedly improved the overall catalytic performance.

3.1.3 Conventional pyrolysis. In conventional pyrolysis, precursors undergo thermal treatment under defined temperature and atmospheric conditions, driving chemical decomposition, atomic redistribution, and phase transformation to form target products. Owing to operational simplicity, modest equipment requirements, and favorable scalability, this method has been widely adopted in defect engineering.[69,70] By judicious selection of precursor species and precise control over pyrolysis parameters-such as the temperature, atmosphere, and heating rate-the type and concentration of defects can be tuned within certain ranges, enabling optimization of catalytic performance.[71] Li *et al.*[68] successfully prepared 2H-MoS_2 nanosheets enriched with V_S by annealing the precursor under a H_2 atmosphere, which resulted in pronounced enhancement in HER activity. EPR measurements were employed to quantitatively track the effect of annealing temperature on vacancy concentration. Gradual increases in point defect concentration were observed as the calcination temperature increased from 400 to 600 °C. However, further temperature elevation induced excessive sulfur loss, leading to formation of large-area defects. In contrast, calcination at 800 °C under an argon (Ar) atmosphere yielded structurally intact trigonal-prismatic MoS_2 crystalline nanosheets (Fig. 3d). This comparison demonstrated that H_2-assisted thermal treatment enables controllable defect introduction over a relatively wide processing window while maintaining good scalability.

Beyond the construction of point defects, conventional pyrolysis can also be employed to fabricate heterojunction electrocatalysts through *in situ* oxidation or nitridation of the host matrix. Zhang *et al.*[72] synthesized Mo_2N/MoO_3@NC-30

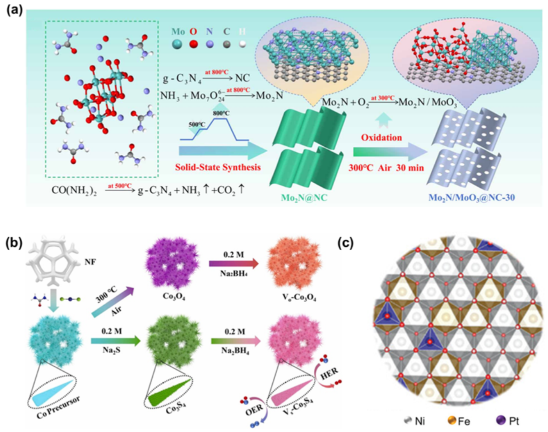

Fig. 4 (a) Schematic diagram of the preparation process for Mo_2N/MoO_3@NC-30 heterojunction catalysts.[72] Copyright 2026 IOP Publishing Ltd. (b) Schematic diagram of the synthesis process of V_O-Co_3O_4@NF and V_S-Co_3S_4@NF.[80] Copyright 2022 Elsevier B.V. (c) Schematic illustration of Pt single-atom-supported α-$Ni_xFe_\gamma(OH)_2$.[81] Copyright 2022 Wiley-VCH.

heterojunction porous nanosheets *via* two-step pyrolysis routes (Fig. 4a). In this process, urea first decomposed at 500 °C under an inert atmosphere to generate carbon nitride and ammonia. The generated ammonia subsequently serves as a nitrogen source to react with the molybdenum precursor at 800 °C, forming Mo_2N. Meanwhile, carbon nitride further decomposed at elevated temperatures to yield nitrogen-doped carbon (NC), resulting in Mo_2N nanoparticles supported on an NC matrix (Mo_2N@NC). On this basis, controlled partial oxidation of Mo_2N at 300 °C produced the Mo_2N/MoO_3@NC-30 heterostructure enriched with interfacial vacancy defects arising from lattice mismatch. XPS analysis demonstrated enhanced interfacial polarization arising from interface defects, which promoted intermediate adsorption and charge transfer. In addition, conventional pyrolysis is widely used to introduce heteroatom dopants such as O, S, F, B, and P into defect-rich electrocatalysts.[73–77] The incorporation of these heteroatoms not only induces defect structures within the lattice but also provides anchoring sites for stabilizing metal active centers. By regulating local electronic distributions, such dopants further optimize reaction kinetics and contribute to enhanced electrocatalytic performance.

3.1.4 Chemical redox methods. Chemical redox methods constitute a class of defect-construction strategies based on electron-transfer reactions. Rational introduction of oxidizing or reducing agents (*e.g.*, H_2O_2 or sodium borohydride) drives redox coupling with active sites, leading to changes in atomic valence states or local chemical environments and indirectly promoting the formation of lattice defects.[78,79] Compared with direct etching or high-temperature treatments, these methods typically operate under milder conditions, offering advantages in the fine regulation of defect structures and electronic states. Wang *et al.*[80] utilized the strong reducing capability of sodium borohydride to introduce anion vacancies into Co_3S_4 under mild conditions (Fig. 4b). DFT calculations revealed that the generated vacancies increased carrier concentration and electrical conductivity while lowering the surface binding energy barriers of reaction intermediates, thereby effectively accelerating reaction kinetics and enhancing overall catalytic activity. In another study, Wang *et al.*[81] employed chloroplatinic acid as a strong oxidant to chemically oxidize α-$Ni_xFe_\gamma(OH)_2$, partially converting Fe species into FeOOH while simultaneously inducing the formation of Fe cation vacancies. During this process, Pt species were stably anchored *in situ* at Fe-vacancy sites *via* oxidation reactions (Fig. 4c). The electron transfer between Pt and α-$Ni_xFe_\gamma(OH)_2$ markedly modulated the local electronic structure, leading to significantly enhanced catalytic performance in both the HER and OER.

3.2 Physical approaches

Physical methods constitute an important class of strategies for defect engineering in electrocatalysts. The fundamental concept lies in breaking the intrinsic chemical bonds and long-range atomic ordered structure of materials through externally applied high-energy fields, thereby inducing lattice defects and modulating the electronic structure and surface reactivity of catalysts. Unlike synthesis routes that rely on chemical reaction pathways, physical methods typically achieve nonequilibrium structural regulation *via* transient energy input, featuring short reaction times, rapid kinetics and the ability to generate diverse defect types.[82–84] Compared with conventional thermal treatments or pyrolysis processes that often require hours or even days, physical irradiation processes can usually be completed within seconds to minutes, making them particularly advantageous for the efficient construction of defect-rich and tunable nano-electrocatalysts.

3.2.1 Physical irradiation methods

3.2.1.1 Plasma treatment. Plasma is a partially ionized gas composed of electrons, ions, excited or ground-state atoms and molecules, free radicals, and photons. It is typically generated by gas discharge at high temperature, or under strong electric fields or high-energy conditions and is regarded as the "fourth state of matter", distinct from solids, liquids, and gases.[85–87] During plasma treatment, energy is transferred to the material surface in the form of ion bombardment or photon irradiation, inducing surface structural reconstruction as the energy dissipates. When high-energy ions interact with surface atoms of the catalyst, energy transfer can cause localized covalent bond breakage and surface atom ejection, thereby generating various vacancies and coordinatively unsaturated sites on the material surface.[88] This makes plasma treatment an effective approach for constructing defect-rich catalysts. Liu *et al.*[89] employed Ar plasma etching to fabricate $NiSe_2$ nanosheet arrays enriched with Se defects. The introduced Se vacancies not only significantly increased the number of HER active sites but also accelerated charge-transfer kinetics by modulating the local electronic structure. Notably, plasma treatment can also enable the simultaneous construction of multiple types of vacancies. Wang *et al.*[88] exfoliated bulk CoFe-LDHs into ultrathin nanosheets using Ar plasma and concurrently introduced O, Co, and Fe vacancies during the exfoliation process (Fig. 5a). These vacancies markedly promoted the adsorption of water

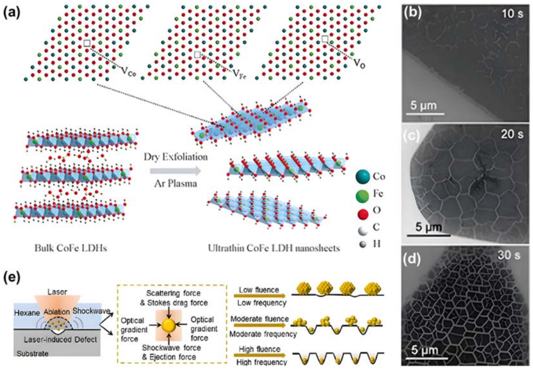

Fig. 5 (a) CoFe LDH nanosheets produced by Ar plasma exfoliation.[86] Copyright 2017 Wiley-VCH. SEM images (b–d) show morphology of monolayer MoS_2 with 10, 20, and 30 s oxygen plasma exposure, where the cracks appear in the basal plane.[90] Copyright 2016 American Chemical Society. (e) Schematic diagram depicting the synthesis of Pt NPs, clusters and SACs under laser planting with low, moderate and high fluences and frequencies, respectively.[101] Copyright 2023 American Chemical Society.

molecules and reaction intermediates. Benefiting from the high specific surface area and abundant exposed active sites enabled by the ultrathin architecture, the obtained material demonstrated excellent OER activity. It should be emphasized that plasma treatment parameters, such as temperature and treatment duration, have a pronounced impact on the structural integrity of materials. At elevated temperatures or extended treatment durations, surface cracking and even structural disintegration became pronounced, as demonstrated by the evolution of basal-plane cracks in monolayer MoS_2 with plasma treatment time (Fig. 5b-d).[90] In order to alleviate the structural degradation induced by high temperatures, Jiang *et al.*[91] employed low-temperature plasma (<500 °C) to simultaneously achieve nitridation, defect construction and interfacial coupling, effectively avoiding phase separation induced by high temperatures. Scanning electron microscope (SEM) and EPR analyses showed severe particle aggregation in untreated $NiSe_2$/Ni/NCNT@CC, whereas plasma-treated catalysts displayed uniformly dispersed nanoparticles and porous architecture, leading to an increased specific surface area of 46.1 $m^2\ g^{-1}$ and providing abundant active sites for electrochemical reactions. Overall, plasma technology features rapid reaction kinetics and a relatively low environmental footprint, which has led to its widespread adoption in defect engineering.[92] However, it should be noted that as a typical surface-modification technique, plasma treatment still faces challenges related to the uniformity of defect distribution during large-scale production.

3.2.1.2 Microwave-assisted methods. Microwave-assisted methods are rapid thermal-treatment techniques based on the interaction between electromagnetic waves and matter, and they have been widely employed in recent years for the construction of defect-engineered electrocatalysts.[93,94] During microwave irradiation, materials with high dielectric loss can undergo rapid and uniform temperature elevation within an extremely short time, followed by instantaneous cooling once the irradiation is terminated. This process enables nonequilibrium structural evolution to occur on the timescale of seconds or even milliseconds.[95] Such "rapid heating-instant quenching" thermal shock readily induces inhomogeneous lattice strain, localized coordination defects, and V_O or V_M within the crystal lattice. Simultaneously, it enables the cooperative promotion of precursor decomposition, elemental doping, and phase-structure reorganization, rendering microwave methods highly efficient for constructing multidimensional defect architectures. According to the physical state of the reaction system, microwave-assisted synthesis can be broadly classified into three main categories: solid-state, liquid-phase, and quasi-solid-state methods. Solid-state microwave-assisted synthesis employs solvent-free solid precursors as the reaction system, typically requiring mechanical grinding or similar processes to ensure homogeneous mixing.[96] Energy absorption relies on the intrinsic dielectric properties of the solids or the presence of added susceptors. Fan *et al.*[97] used urea as a nitrogen source to synthesize O/N co-doped commercial conductive carbon (ONCB) in a household microwave oven *via* a 40 s rapid irradiation process. This strategy not only introduced abundant oxygen- and nitrogen-containing functional groups but also generated numerous defects and porous structures within the carbon framework, thereby promoting the uniform dispersion of Ru nanoparticles on the support. However, due to limitations in solid-state diffusion, localized overheating may occur, making precise temperature control challenging. In contrast, liquid-phase microwave-assisted synthesis employs polar solvents such as water, alcohols or ionic liquids as reaction media. Upon dissolution of the precursors, homogeneous or multiphase reaction systems containing mobile dipoles and ions are formed, which enables efficient microwave energy transfer through dipolar rotation and ionic conduction mechanisms. Compared with solid-state approaches, liquid-phase microwave synthesis generally offers more rapid volumetric heating and a faster mass transfer rate. Alam Khan *et al.* achieved the rapid synthesis of TiO_2 gel spheres by microwave treatment of a biphasic system consisting of polymeric titanium ethoxide dispersed in kerosene, pioneering liquid-phase microwave synthesis of inorganic materials.[98] Owing to its versatility and controllability, this strategy has become the most widely applied microwave-assisted synthesis route. In practice, the scalability of this method is limited, thereby hindering its large-scale application.

Situated between solid-state and liquid-phase approaches, quasi-solid-state microwave synthesis has recently attracted increasing attention as a transitional strategy. In this approach, small quantities of solvent are incorporated to transform the precursors into a semi-solid or paste-like state. This configuration improves thermal uniformity in solid-state systems and is conducive to large-scale application. Using quasi-solid-state microwave methods, Wu *et al.* achieved the effective coupling of low loadings of noble metals with transition-metal oxide, carbide and hydroxide matrices, successfully constructing a series of electrocatalysts enriched with V_O,[55,93,94] which exhibited favorable catalytic activity and stability. Despite the pronounced advantages of microwave-induced thermal shock in defect construction, significant challenges remain in terms of process controllability and scalability, which continue to limit its large-scale implementation.

3.2.1.3 Laser-assisted methods. Laser-assisted synthesis is an advanced physical approach that relies on ultrashort interaction time and ultrahigh power density. In this process, high-energy laser pulses are delivered to materials within an exceptionally short duration, inducing localized chemical bond cleavage and thereby generating various defect structures.[99,100] The type and concentration of defects generated during laser-assisted synthesis are strongly dependent on laser parameters, including fluence, pulse width and scanning mode. Zou *et al.*[101] proposed a laser implantation strategy for the universal preparation of high-loading SACs (Fig. 5e). Specifically, laser pulses concurrently generated substrate defects and isolated metal atoms, with the defect sites serving as effective anchors through enhanced electronic interactions.

Their study demonstrated that increasing laser fluence markedly enhanced bond rupture and local energy fluctuations, thereby facilitating the migration of metal atoms into lattice interstitials or inducing the formation of abundant surface and bulk vacancies. Thus, the metal loading of SACs reached a record-high level of 41.8 wt%. In addition, laser techniques enable effective regulation of the catalyst morphology and microstructure. Gary J. Cheng and co-workers[102] constructed a laser shock-induced nanoreactor through precise regulation of the experimental setup and laser parameters, thereby enabling directional control over the reaction process and successfully fabricating coral-like LDH substructures featuring an ultrahigh specific surface area, abundant defects, and uniformly distributed dopants (Fig. 6a and b). Using this approach, layered double hydroxide nanosheets with a thickness of approximately 3 nm were obtained, representing ∼75% reduction compared with those synthesized *via* conventional solvothermal methods. This strategy effectively overcomes the limitations associated with insufficient morphological control in laser-based fabrication of layered materials.[103] The above synthetic strategies are predominantly focused on the preparation of defect-rich catalysts *via* laser ablation in liquid environments. Notably, this approach is not limited to liquid-phase systems and can also be extended to solid-state conditions for defect engineering. Using a mixture of indium chloride and carbon nanotubes as the precursor, Ye *et al.*[104] employed the transient laser-assisted strategy to rapidly generate In-based catalysts (L-In) featuring abundant stacking faults, vacancies, and interstitial defects (Fig. 6c). The synergistic coexistence of these defects significantly enhanced the activity and selectivity of the catalysts toward the CO_2 reduction reaction.

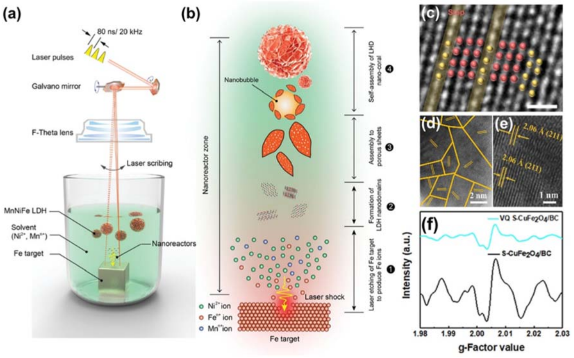

Fig. 6 (a) The illustration of the experimental set-up for the synthesis of a LDH nano-coral.[102] Copyright 2022 Wiley-VCH. (b) The illustration of the laser-induced nanoreactor.[102] Copyright 2022 Wiley-VCH. (c) Spherical aberration corrected HRTEM images of L-In showing the defects such as vacancies, interstitial atoms and stacking faults.[104] Copyright 2022 Wiley-VCH. (d and e) TEM and HRTEM images for GB-$(Fe_{0.66}Co_{0.34})_2B$.[108] Copyright 2022 Elsevier B.V. (f) EPR spectra of S–$CuFe_2O_4$/BC and VQ S–$CuFe_2O_4$/BC.[109] Copyright 2024 American Chemical Society.

3.2.2 Ball-milling method. Ball milling is a representative mechanically driven synthesis technique that has been extensively applied to defect construction and structural modulation of transition-metal-based electrocatalysts. Its fundamental mechanism involves continuous high-frequency collisions, friction and shear between milling balls and precursor materials, which induce lattice distortion, structural disordering and the formation of surface and interfacial defects.[105–107] Compared with thermally or chemically driven synthetic approaches, ball milling enables extensive structural reconstruction under ambient or near-ambient conditions and is therefore particularly effective in generating high densities of GBs and edge defects. Qin *et al.*[108] synthesized intermetallic GB-$(Fe_xCo_{1-x})_2B$ OER catalysts with tunable GBs densities *via* high-energy ball milling of Fe/Co/B powders using zirconia balls as the milling medium (Fig. 6d and e shows the GBs density). DFT calculations combined with electrochemical measurements demonstrated a significant increase in accessible active sites with increasing GBs density. Meanwhile, the incorporation of Fe effectively modulated the adsorption configurations and reaction pathways of key intermediates, synergistically promoting efficient OER performance. Beyond single-defect engineering, ball milling also enables the simultaneous construction of multiple defect types. Song *et al.*[109] employed sulfur powder as the dopant source and synthesized S–$CuFe_2O_4$/BC catalysts featuring dual-vacancy defects *via* high-speed ball milling. Scanning transmission electron microscopy (STEM) images showed pronounced wrinkling and cracking at the edges of $CuFe_2O_4$/BC nanoparticles after milling, accompanied by discontinuous lattice fringes and evident interfacial dislocation defects. XAS and EPR analyses further demonstrated an increased V_O concentration upon sulfur doping, accompanied by partial substitution of O_L by sulfur atoms. Under sustained mechanical compression, V_S were simultaneously generated (Fig. 6f). These defects endowed metal sulfides with high lattice distortion energies and flexible atomic rearrangement capabilities, leading to extensive exposure of active sites and accelerated electrocatalytic kinetics. Overall, ball milling offers advantages such as process simplicity, broad precursor compatibility and scalability, and is therefore well suited for the preparation of defect-rich electrocatalytic nanomaterials.[110] Nevertheless, relatively high energy consumption, together with limited control over defect types and spatial distributions, continues to constrain the practical application of this approach.

4 Dynamic evolution of defects

In existing studies, the characterization and analysis of defects have predominantly relied on *ex situ* characterization techniques, which focus on elucidating how defects in relatively stable structural states regulate catalytic performance, thereby laying the foundation for establishing structure–performance relationships between defects and catalytic behavior. However, accumulating experimental evidence indicates that defects undergo dynamic evolution processes under synthesis and realistic reaction conditions prior to establishing definitive structure–property relationships.[111,112] This approach facilitates more comprehensive understanding of defect formation processes and their underlying mechanisms. Investigating the dynamic evolution of defects during the synthesis stage benefits the elucidation of their formation pathways and stabilization mechanisms, thereby providing a solid foundation for the controllable construction of defects. In contrast, probing defect dynamics under electrocatalytic operating conditions helps to elucidate the mechanisms underlying the generation, transformation and deactivation of active sites under realistic reaction conditions, deepening the understanding of intrinsic electrocatalytic processes. Overall, defect dynamic evolution is an intrinsic property of defect-rich electrocatalysts, and understanding its driving forces and evolution pathways is fundamental to elucidating the true working-state structure of catalysts. Furthermore, elucidating the dynamic evolution behaviours of defects is a prerequisite for achieving their precise and controllable regulation. In the following sections, we systematically analysed the driving forces and typical pathways of defect dynamic evolution under electrocatalytic conditions.

4.1 Driving forces for defect dynamic evolution

The dynamic evolution of defects in catalysts is typically governed by the synergistic effects of thermodynamic, electrochemical, mechanical, and chemical environments. Given that defects inherently reside in high-energy and metastable states, their structures are highly susceptible to reconstruction in these complex environments, enabling dynamic optimization of the electronic structure and electrocatalytic performance.

Among the various driving forces, thermodynamic effects play a fundamental and decisive role. Elevated temperature enhances atomic mobility, thereby accelerating defect formation, diffusion, aggregation and order-disorder transitions. Under relatively low-temperature conditions (*e.g.*, ∼300 °C), limited atomic mobility favored energetically stable ordered configurations of V_O, such as the Cu_4O_3 (corresponds to the CuO phase containing 25% ordered V_O) superstructure formed at the subsurface of CuO.[113] In contrast, entropy-driven processes governed defect behavior at elevated temperatures on the order of 900 °C, leading to defect disordering and vacancy diffusion into the bulk, ultimately leading to the formation of subsurface one-dimensional V_O channels in CeO_2.[114] Beyond thermal energy input, mechanical actions, such as localized high temperatures (>1000 °C) generated during ball milling, could induce substantial oxygen displacement in catalysts such as ZnO_{1-x}/Cu, resulting in a high concentration of V_O (Fig. 7a). Correspondingly, Zn 2p peaks at 1021.8 and 1044.8 eV corresponded to Zn $2p_{3/2}$ and Zn $2p_{1/2}$, and Zn LMM auger electron spectroscopy spectra (LMM AES spectra) features at 988.8 and 992 eV were assigned to Zn^{2+} and $Zn^{\delta+}$ ($\delta < 2$) (Fig. 7b), confirming that there existed some reduced Zn species, indicating the presence of V_O.[115] Moreover, severe lattice distortions[116] represent localized thermodynamic instabilities that tend to promote defect aggregation and are often accompanied by the formation of bulk defects. At the macroscopic level, thermodynamic parameters including GBs curvature, interfacial energy and reaction barriers collectively drive GBs migration to minimize the total free energy of the system.[117] These observations collectively indicate that thermodynamic driving forces govern the dynamic evolution of defects in electrocatalysts throughout the entire process and operate across multiple length scales.

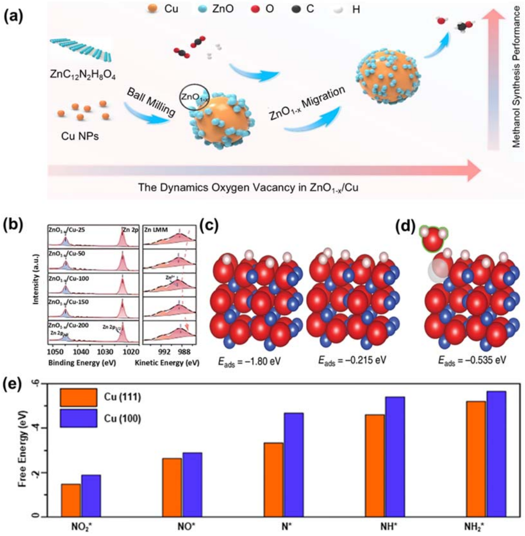

Fig. 7 (a) Schematic illustration of the synthesis of ZnO_{1-x}/Cu.[115] Copyright 2024 American Chemical Society. (b) Zn 2p XPS and Zn LMM AES spectra of the reduced ZnO_{1-x}/Cu catalysts.[115] Copyright 2024 American Chemical Society. (c) The lowest-energy configuration of stable OH groups formed by H adsorption on the CuO surface.[124] Copyright 2020 Springer Nature. (d) The adsorption of the 6th H atom triggers the spontaneous desorption of H_2O and the formation of V_O on the CuO surface.[124] Copyright 2020 Springer Nature. (e) Comparing the free adsorption energy of different nitrate reduction (NO_3^-RR) intermediates on the structural models of Cu (111) and Cu (100).[125] Copyright 2021 Royal Society of Chemistry.

As one of the most critical external stimuli in electrocatalytic systems, electric fields or applied bias can also regulate the direction and rate of defect migration through directional energy input, thereby profoundly influencing catalytic performance. In TiO_2 systems, the application of an external bias induced the "dragging effect" that drove subsurface V_O toward the surface, where they aggregated into clusters consisting of two to three vacancies.[118] Furthermore, progressive oxidation of metal ions to high-valence states under anodic polarization generates local charge imbalance, which weakens M–O bonds and accumulates lattice stress, thereby facilitating the formation of V_O and V_M. These vacancy defects modulate the band structure and local electronic structure, promoting reactant adsorption and activation.[38,119] Nevertheless, with further increases in current density and potential, enhanced electron-transfer rates and elevated surface atomic kinetic energy facilitate defect migration and aggregation, which may induce bulk phase transformations or even structural collapse of the catalyst.[120] For instance, Wang *et al.*[121] introduced Cr and V into FeCoNi/CC to modulate the electronic structure. During the OER, Cr and V acted as sacrificial dopants and underwent controlled dissolution, generating abundant *in situ* V_O and significantly increasing the density of active sites. This process represented a typical defect-engineering strategy in high-entropy systems, where selective element leaching could dynamically regulate defect concentration and surface reconfiguration. Despite partial Cr/V dissolution, the remaining high-entropy alloy retained high configurational entropy, effectively suppressing phase separation and maintaining structural integrity. Such entropy-stabilized frameworks are widely recognized as a key advantage of high-entropy materials for accommodating defect formation while preserving phase stability under specific reaction conditions.

Beyond external fields, reaction intermediates generated during catalysis can be regarded as "molecular switches" governing defect dynamic evolution. Strong adsorption of intermediates often introduces substantial local stress or induces charge redistribution at the atomic scale, thereby triggering atomic rearrangements and leading to the transient formation or healing of defects.[122,123] Such dynamic adaptation is widely considered as an intrinsic origin of high catalytic activity. Specifically, V_O gradients introduced by surface reactions, such as OH/H_2O adsorption–desorption, can drive defect diffusion into the subsurface region and induce dynamic order-disorder structural oscillations. For example, Zhou *et al.*[124] investigated the accumulation adsorption of H on CuO surfaces and the subsequent formation of H_2O using DFT (Fig. 7c and d). Sustained adsorption of H atoms led to the formation of surface OH groups, which remained stable on the surface up to an OH coverage of 0.625 monolayers. Upon further H adsorption, H atoms bound to the surface OH groups and formed H_2O molecules, which desorbed from the surface in a barrier-less manner. This H_2O desorption process resulted in O_L depletion and concomitant generation of V_O on the oxide surface. The vacancies subsequently diffused into the subsurface, thereby disrupting the ordering of the Cu_4O_3 superstructure. The subsequent re-accumulation of surface OH species promoted vacancy reordering, ultimately giving rise to a periodic structural transformation process. Guided by this understanding, He *et al.*[125] exploited *N intermediates generated during NO_3^-RR as capping agents to control the growth of Cu-based nanocrystals with dominant Cu (111) facets, successfully obtaining highly active catalysts enriched with Cu (100) facets and surface defects (Cu (100) exhibited higher activity toward the NO_3^-RR among the two facets).

DFT calculations revealed that the synergistic exposure of Cu (100) facets and surface defects enhanced the adsorption of both *NO_3 and *H, lowering the reaction barrier for the NO_3^-RR, while effectively suppressing the competing HER (Fig. 7e). In summary, driven by the cooperative effects of thermodynamic, electrochemical, mechanical and reaction chemical environments, catalyst defects undergo continuous self-adaptive dynamic evolution, achieving a delicate balance between activity enhancement and structural stability. This understanding not only deepens fundamental insights into defect-mediated catalytic mechanisms but also provides a solid theoretical basis for the rational design of high-performance electrocatalysts through the emerging paradigm of "defect regulation under specific reaction conditions".

4.2 Typical pathways of defect dynamic evolution

Under the continuous influence of external stimuli, the dynamic evolution of defects in materials typically proceeds along several key pathways, including defect generation and healing, defect migration and aggregation and defect-induced structural reconstruction. These dynamic pathways define the continuous evolution of defects from their initial formation to their actual working states, providing a comprehensive framework for elucidating the mechanisms governing defect regulation.

Dynamic defect generation constitutes the initial stage of this evolutionary process. Esch *et al.*[114] systematically investigated the formation and time-dependent evolution of V_O on CeO_2 surfaces, using high-temperature vacuum annealing to induce vacancy formation and employing scanning tunneling microscopy (STM) in combination with DFT calculations for structural and mechanistic analysis. In the early stages of annealing, CeO_2 (111) surfaces were primarily populated by isolated V_O, which could stably occupy either surface or subsurface positions with comparable coverages. According to theoretical calculations, V_O introduced localized electrostatic perturbations that promoted lattice relaxation, charge redistribution and the reduction of neighboring Ce ions to Ce^{3+}, ultimately leading to localized structural distortions. With prolonged annealing, initially isolated V_O gradually migrated and interacted with one another, exhibiting pronounced tendency toward spontaneous aggregation. STM observations showed that short-chain vacancy clusters formed first and subsequently evolved into extended chain-like defect structures composed of multiple vacancy units, including double-chain and triple-chain configurations. These results indicate that individual defects possess an intrinsic propensity to aggregate into vacancy clusters under thermodynamic driving forces and charge reorganization, while the continuous aggregation process is often accompanied by further reconstruction of local atomic structures and electronic states.

Furthermore, the continuous accumulation of defects not only alters the local electronic structure of materials but can also triggers pronounced lattice reconstruction, thereby inducing the dynamic annihilation and redistribution of defects. With CuO as a model system,[113] *in situ* TEM studies showed that lattice collapse was induced when the V_O concentration exceeded the accommodation limit of local superstructures, enabling efficient vacancy annihilation. Specifically,

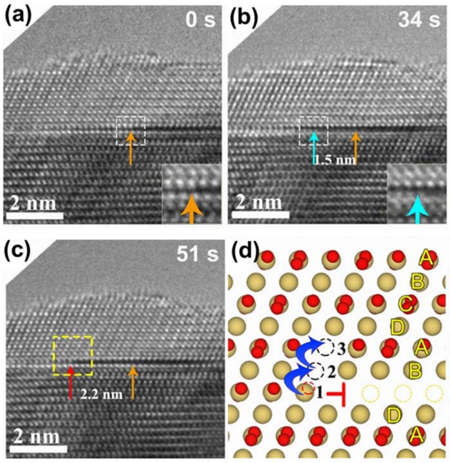

Fig. 8 (a–c) Time-resolved HRTEM images of CuO at p(H_2) ≈ 0.5 Pa and T ≈ 300 °C showing that a stacking fault in the bulk propagates laterally toward the left.[113] Copyright 2021 American Chemical Society. (d) Atomic model of the stacking fault and migration of a Cu atom from site 1 to site 2 and then to site 3, leading to propagation of the stacking fault upon the aggregation of the V_O in the Cu–O plane.[113] Copyright 2021 American Chemical Society.

excessive V_O formation led to the localized collapse of subsurface Cu–O layers, giving rise to stacking-fault structures within the crystal. HRTEM snapshots (Fig. 8a-c) clearly captured the lateral propagation of stacking faults generated by the collapse of subsurface Cu–O layers (marked by the orange, cyan and red arrows). From a crystallographic perspective, the CuO lattice consisted of alternately stacked Cu–O layers and Cu atomic layers. When the specific Cu–O layer collapsed owing to excessive V_O accumulation, structural defects such as edge dislocations were introduced into the lattice. DFT calculations further confirm that the sustained accumulation of V_O significantly destabilized the Cu–O coordination environment, rendering Cu atoms severely undercoordinated and thereby driving their migration toward intrinsic Cu vacancy sites in adjacent layers (Fig. 8d). This process directly illustrated the coupled dynamic evolution of defect migration, aggregation and annihilation. Such structural transformations ultimately exerted a direct influence on the catalytic performance of defect-engineered catalysts.

At a higher level, phase transitions can be regarded as an advanced manifestation of defect evolution. By disrupting the ideal periodicity of the crystal lattice, phase transitions introduce localized strain accumulation and energy fluctuations, providing favorable nucleation sites and lower-energy pathways for the emergence of new phases.[126,127] Conversely, phase transitions are inherently coupled with defect generation and annihilation, owing to the proliferation of interfaces, dislocations, and other defect structures during new-phase formation.[128] This dynamic interplay between defects and phase transitions is widely recognized as a key factor governing the material structure and performance. For example, Mn doping induced Jahn–Teller (J–T) distortions that caused pronounced deformation of MnO_6 octahedra centered on Mn, generating V_O, coordination unsaturation and other types of defects. These defects substantially lowered the phase-transition energy barriers from Co_4N to Co_3O_4, CoOOH and ultimately CoO_2, accelerating the generation of LOM-relevant high-valence metal active species. Nitrogen desorption and the increase in Co oxidation states further promoted the generation of new defects during the phase-transition process. In turn, these defects regulate local electronic configurations and lattice stability, effectively suppressing the aggregation of phase-transition products while maintaining continuous exposure of active sites.[129]

5 Capturing defects

To verify the mechanisms of defect dynamic evolution and overcome the limitations of conventional *ex situ* characterization, advanced *in situ*/*operando* techniques are indispensable. Conventional defect characterization primarily relies on structural, compositional and electronic-structure analysis techniques to elucidate the types and functional roles of defects in materials across multiple length scales. At the crystallographic level, XRD is widely employed to identify lattice distortion and variations in long-range order. Features such as peak shifts, broadening and asymmetry are commonly regarded as indirect indicators of strain accumulation and dislocation introduction.[130] Raman and Fourier-transform infrared (FTIR) spectroscopies are sensitive to short-range order and local bonding environments, enabling the identification of defect-induced local structural perturbations *via* variations in vibrational peak positions and intensities.[131] At microstructural and atomic scales, electron microscopy techniques allow the direct observation of diverse defect structures, ranging from dislocations and grain boundaries to stacking faults, amorphous regions, and heterogeneous interfaces.[132] Of these, STEM imaging allows for the direct observation of most 0D and 1D defects. This technique is also applicable to semi-quantitative analysis of defect concentrations, where statistical counting of defects within localized regions, combined with appropriate extrapolation, enables estimation of the overall defect density in the material.[133] The chemical composition and electronic structure are commonly probed using XPS for surface valence, vacancy, and doping analysis, while EPR provides complementary insight into defect-related species and low-coordination metal sites owing to its high sensitivity to unpaired electrons.[134] Among them, XPS can be employed for the indirect identification and semi-quantitative analysis of 0D and 2D defects. For instance, detailed deconvolution of the O 1s spectra across different samples allows for the relative quantification of V_O concentrations.[135] Moreover, energy-dispersive X-ray spectroscopy (EDS) enables compositional analysis by analyzing the cation/anion stoichiometric ratios and can be used to estimate defect concentrations; however, the results are generally semi-quantitative and lack absolute quantitative accuracy.[133] Overall, although these techniques provide critical insights into defect configurations and structural characteristics, they are largely limited to "static" analyses before and after the reaction, and thus insufficient for capturing the real-time evolution of defects during formation and under working conditions. Consequently, *in situ* and *quasi-in situ* characterization techniques have emerged as major development directions in defect research. Accurate and real-time characterization of defects is the key support for the precise construction and controllable regulation of defects, and conventional and *in situ*/*operando* characterization techniques for defect detection and dynamic evolution monitoring are summarized in this section.

Conventional electron microscopy generally provides only static snapshots of defects before and after the reaction, whereas key processes such as defect generation, evolution, healing and annihilation under realistic operating conditions remain largely inaccessible. *In situ* electron microscopy overcomes this limitation by precisely reproducing catalytic reaction environments within the microscope chamber, enabling real-time visualization of catalyst evolution from the atomic to nanometer scale and revealing dynamic correlations between defect evolution and catalytic activity enhancement.[136–138] For example, Patrick R. Unwin *et al.*[139] employed scanning electrochemical cell microscopy (SECCM) to generate potential-dependent electrochemical "videos" under H_2 and CO_2 atmospheres, simultaneously mapping the electrocatalytic activity distribution and surface topography of gold electrodes. By combining these measurements with high-resolution electron backscatter diffraction (HR-EBSD), grain orientation, lattice strain and dislocation density maps were constructed (Fig. 9a). The results showed that dislocations were enriched near GBs, which likely accounted for the enhanced localized catalytic activity previously observed at these sites. Moreover, dislocations also tend to aggregate at other structural features, such as slip bands (SBs), thereby giving rise to multiple potential localized regions of high catalytic activity within the material. Guo *et al.*[140] further integrated *in situ* electrochemical atomic force microscopy with scanning electrochemical microscopy (EC-AFM-SECM) to synchronously track nanoscale morphological evolution and local catalytic activity (Fig. 9b). Under *operando* conditions, they clarified the spatial distribution and dynamic formation of defect sites, demonstrating that surface reconstruction of amorphous SnO_2/GO catalysts during the NO_3^-RR induced the proliferation of edge- and wrinkle-like defects, which were identified as catalytic "hot spots". This technique establishes dynamic and causal linkage between microstructural evolution and macroscopic performance, substantially advancing materials research from empirical exploration toward rational design. Benefiting from the highly disordered intrinsic structure, amorphous materials underwent dynamic bond rearrangement under specific reaction conditions, thereby enabling continuous regeneration of active defects.

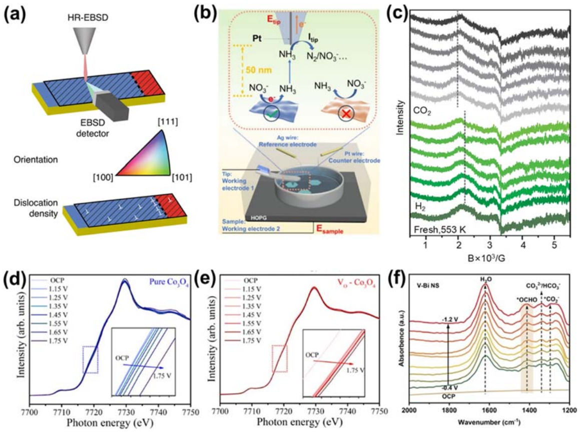

Fig. 9 (a) The dislocation density schematic on the surface of the gold electrode.[139] Copyright 2021 Springer Nature. (b) Schematic diagram of the EC-AFM-SECM setup for evaluating the NO_3^-RR responsiveness of the catalyst.[140] Copyright 2025 American Chemical Society. (c) *In situ* EPR spectra of the 0.75Pd–5In_2O_3–ZrO_2 catalyst prepared.[145] Copyright 2022 Springer Nature. *Operando* XAS of the Co K-edge of (d) pure Co_3O_4 and (e) V_O-Co_3O_4. The insets show magnified views of the regions marked by dotted boxes.[149] Copyright 2020 American Chemical Society. (f) *In situ* ATR-FTIR spectra of V-Bi NS at different potentials.[155] Copyright 2024 Wiley-VCH.

In situ EPR/electron spin resonance (ESR) is among the most powerful techniques for directly probing the dynamic evolution of defects in electrocatalysts.[141,142] This method selectively detects signals originating from defects containing unpaired electrons, such as $V_{O/M}$ and dangling bonds. By monitoring signal intensity changes at characteristic *g*-factor positions as potential or time varies, the evolution of specific defect concentrations can be directly and quantitatively evaluated,[143] establishing a direct link between electrochemical stimuli and defect generation or annihilation kinetics. Gunnar Jeschke and co-workers[144,145] systematically investigated the evolution of V_O in ZrO_2-supported In_2O_3/ZnO-based catalytic systems using the *in situ* EPR technique, including both pristine materials and those doped with Cu, Pd, and Ni. Under a flowing H_2 atmosphere, vacancy-related signals were observed to broaden progressively with increasing time, which was attributed to the continuous generation of additional V_O. Upon subsequently switching the gas atmosphere to CO_2 and maintaining it for 2 h, the vacancy signals gradually narrowed, indicating that part of the newly formed defects was partially healed under oxidizing conditions (Fig. 9c). These observations provide compelling evidence that V_O undergo pronounced dynamic evolution.

During electrocatalytic reactions, *in situ* XAS enables real-time monitoring of metal oxidation states and local coordination environments, thereby directly elucidating how defects respond to applied potentials, interact with reaction intermediates and ultimately govern catalytic performance.[146–148] For instance, Wang *et al.*,[149] by tracking the evolution of Co coordination environments, demonstrated that V_O do not act as direct OER active sites but instead follow the dynamic pathway of "OH capture → induced Co pre-oxidation → Co–OOH formation", effectively lowering the reaction energy barrier (Fig. 9d and e). Zhao *et al.*[150] revealed *via in situ* XAS that the absorption edge shifted to the low-energy region at 1.25 V, indicating a decrease in the valence state of Ni sites. Upon increasing the potential to 1.35 V, the Ni sites were oxidized to higher valence states, resulting in a gradual shift of the absorption edge toward the high-energy region. The variation of *operando* XAS spectra was attributed to the structural distortion of lower symmetry unsaturated Ni sites by adsorption of OH^- and removal of the terephthalic acid (BDC) ligand at low potential, and evolution to a highly symmetric NiO_6-liganded

Table 1 Comparison summary of representative studies

Catalyst	Synthesis methods	Defect types	Target reactions	Performance metrics	Relevant mechanisms	Ref.
V_{Cr},Co–NiFeOOH	Corrosion and electrochemical self-activation	Cation vacancy	OER in 1 M KOH	198 mV @ 10 mA cm^{-2}	Local electronic structure optimization and surface adsorption energy modulation	162
NiFeCe-LDH@CP	Hydrothermal method	Doping defects	OER in 1 M KOH	267 mV @ 100 mA cm^{-2}	Local electronic structure optimization and surface adsorption energy modulation	32
Ni,B–RuO_x	Solid-liquid reaction and annealing	Doping defects	OER in 0.5 M H_2SO_4	206.8 mV @ 10 mA cm^{-2}	AEM-LOM coupling mechanism and grain boundary-bulk synergy	180
W–NiCo_2O_4	Electrodeposition and annealing	Doping defects	OER in 0.5 M H_2SO_4	206.8 mV and stable operation for 100 h (10 mA cm^{-2})	Dynamic oxygen replenishment mechanism, local electronic structure modulation, and V_O healing	181
Mo_2N/MoO_3@ NC-30	Annealing	Heterointerface defects	HER in 1 M KOH	94 mV @ 10 mA cm^{-2}, stable operation for 1000 h at 500 mA cm^{-2}	Interfacial polarization effect and interfacial electron delocalization and accumulation	72
IrNi/F-MWCNTs	Thermal shock	Doping defects	HER in 1 M KOH	31 mV @ 10 mA cm^{-2}	Interfacial water restructuring and d-band center theory	188
MoO_{3-x}/Mo_2AlB_2	Hydrothermal method and intercalation	Mixed defects	HER in 0.5 M H_2SO_4	38 mV @ 10 mA cm^{-2}	Active microdomains theory and electronic structure modulation	199
V–Ni^{II}–Fe	Impregnation	Vacancy	OER in 1 M KOH + seawater	333 mV @ 1 A cm^{-2}	V_O-induced Ni^{4+} formation mechanism and the selective adsorption effect of hard acids	218

octahedron (β-NiOOH) at high potential. And β-NiOOH would further generate some V_O (V_O–NiOOH) to promote the reaction under potential application, intuitively capturing the dynamic evolution behavior of defects.

Raman and infrared spectroscopies are highly sensitive to molecular vibrational modes, and variations in defect states often induce pronounced changes in surface bond vibrational frequencies. Consequently, these techniques not only allow quantitative evaluation of defect density and type through enhancement of defect-related vibrational features,[151] but also enable sensitive detection of key reaction intermediates at defect sites, thereby elucidating the role of defects in stabilizing intermediates and optimizing reaction pathways.[152,153] For example, Li *et al.*[154] identified the presence of initial V_M through characteristic peak assignments in *in situ* Raman spectra, and further revealed the dynamic evolution of V_M ($V_M \rightarrow V_{MOH} \rightarrow V_{MOH\text{-}H}$). Zhang *et al.*[155] employed *in situ* attenuated total reflection-Fourier transform infrared spectroscopy (ATR-FTIR) to capture signals of key intermediates ($^*CO_2$ and *OCHO). The vacancy-containing catalyst enabled the detection of relevant signals at lower potential compared with the vacancy-free control catalyst, demonstrating that vacancy defects enhanced adsorption and activation of inert CO_2 molecules *via* their electron-rich nature (Fig. 9f). Vacancy defects could also stabilize the adsorption of the key intermediate *OCHO, thus facilitating the reaction kinetics of formate production.

In addition, several other *in situ* techniques have been widely applied to monitor defect evolution. The synergistic application of these techniques provides a comprehensive experimental framework for elucidating the formation and dynamic evolution mechanisms of defects in electrocatalysts.

6 Applications of defect engineering in water electrolysis

Defect engineering has become a core strategy for regulating the electronic structure and surface reaction environment of electrocatalysts, and has been widely applied across various electrocatalytic systems. Among these, water splitting is considered as a representative model system for elucidating the role of defect engineering, owing to its well-defined reaction pathways, well-established mechanistic understanding, and significant industrial relevance.[156] Accordingly, defect engineering has been particularly extensively explored in the HER and OER, and has emerged as a key strategy for enhancing electrocatalytic performance. Unlike conventional strategies such as morphology regulation or compositional optimization, defect engineering typically avoids extensive modification of the bulk crystalline framework. Instead, it introduces localized structural imperfections to precisely tailor electronic states, coordination environments, intermediate adsorption energetics and reaction pathways. In this context, this section systematically reviews the dynamic modulatory roles and underlying mechanisms of several representative defect types, namely vacancy defects, doping-induced defects, and heterointerface defects, in conventional and complex water electrolysis systems (Table 1).

6.1 Conventional electrolysis system

6.1.1 Alkaline OER. In alkaline OER, the mismatch in adsorption strengths of key reaction intermediates (*OH, *O, and *OOH), together with the intrinsic linear scaling relationships among these species, often results in high reaction overpotentials for most catalytic systems.[157] Although LOM has been proposed as a promising route to overcome the intrinsic scaling limitations of AEM, the controlled activation and sustained involvement of O_L remain poorly understood. During extended OER operation, structural reconstruction, such as metal dissolution and O_L participation, can transiently enhance catalytic activity. However, this dynamic evolution is often accompanied by irreversible structural degradation, which ultimately limits stable operation at industrially relevant current densities.[158–160] Moreover, bubble coverage-induced interfacial mass transport limitations further exacerbate these issues and accelerate performance decay at high current densities.[161] Overcoming these inherent bottlenecks remains central to advancing alkaline OER research. In this context, defect engineering offers new opportunities to modulate intermediate adsorption energetics and stabilize dynamically evolving catalytic structures during operation.

Vacancy defects engineering (*e.g.* V_O and V_M) are widely regarded as among the most direct and effective strategies for tuning OER activity. By modifying the local atomic coordination environment, vacancy defects can reconstruct intermediate adsorption behavior and thereby optimize overall reaction kinetics. Guo *et al.*[162] constructed Cr-vacancy-rich catalysts (V_{Cr},Co–NiFeOOH) *via* two-step strategies involving room-temperature corrosion and subsequent electrochemical self-activation. DFT calculations based on the extended microenvironment model comprising approximately 40 metal atoms demonstrated that the introduction of V_{Cr} markedly weakened the adsorption of reaction intermediates on adjacent Fe sites (Fig. 10a), thereby alleviating excessive adsorption. In synergy with Co sites, this vacancy-induced modulation enabled fine-tuning and spatial redistribution of surface adsorption energetics. As a result, the energy barrier of the OER RDS decreased from 2.34 eV to 2.20 eV, markedly accelerating the kinetics of the critical reaction step. Beyond the surface regulation of adsorption energy, vacancies formed dynamically could activate O_L by enhancing M–O covalency, facilitating mechanistic transitions and inducing *in situ* reconstruction of the active phase. Based on this strategy, He *et al.*[163] systematically compared the electrochemical reconstruction behaviors of crystalline NiMoO (hc-NiMoO) and amorphous NiMoO (a-NiMoO, usually with various defects[164]) during the OER, elucidating the intrinsic correlation between "covalency-reconstruction-activity". *In situ* Raman spectroscopy demonstrated the disappearance of M–O vibrational modes and the emergence of characteristic Ni–OOH peaks in a-NiMoO at ~1.40 V, while the same structural evolution in hc-NiMoO required a higher potential of ~1.60 V (Fig. 10b and c). Further analysis of the $\delta(Ni^{3+}–O)/\nu(Ni^{3+}–O)$ ratio

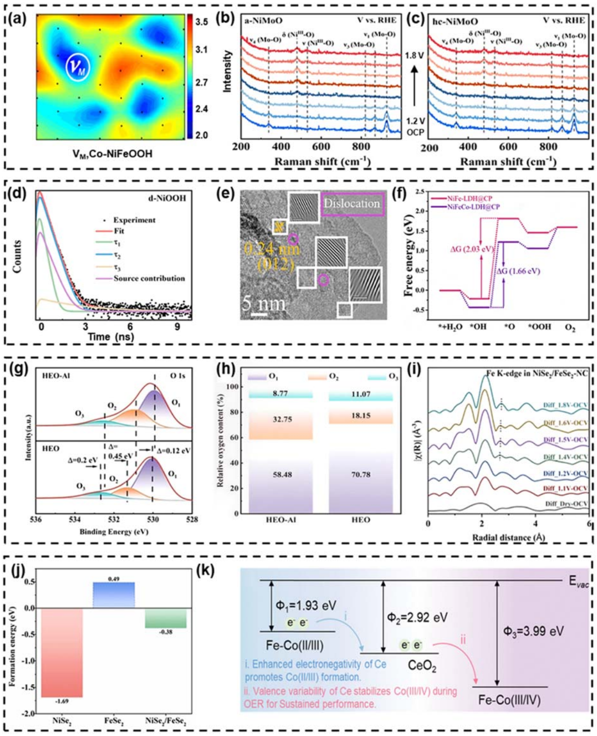

Fig. 10 (a) Reallocation of adsorption energy with a uniform mixture of local relatively high and low states.[162] Copyright 2025 American Chemical Society. *In situ* Raman spectra of (b) a-NiMoO and (c) hc-NiMoO.[163] Copyright 2025 Wiley-VCH. (d) Measured lifetime spectrum of d-NiOOH by the PAS test.[163] Copyright 2025 Wiley-VCH. (e) HRTEM image of NiFeCe-LDH@CP.[32] Copyright 2023 Elsevier B.V. (f) Gibbs free energy diagram for the four steps of the OER on NiFe-LDH@CP and NiFeCe-LDH@CP.[32] Copyright 2023 Elsevier B.V. (g and h) O 1s XPS spectra of HEO-Al and HEO catalysts, along with their corresponding relative oxygen contents.[166] Copyright 2025 American Chemical Society. (i) *In situ* XAS spectra of $NiSe_2/FeSe_2$-NC.[169] Copyright 2023 Elsevier B.V. (j) Formation energy of Se vacancies in $NiSe_2$, $FeSe_2$ and $NiSe_2/FeSe_2$.[169] Copyright 2023 Elsevier B.V. (k) Proposed nature of $\Delta\Phi$ during the OER in CeO_2/Fe–Co$(OH)_2$ catalysts.[170] Copyright 2025 Royal Society of Chemistry.

indicated that a-NiMoO preferentially transformed into disordered d-NiOOH, while hc-NiMoO evolved into relatively ordered *o*-NiOOH, suggesting an enhanced propensity of amorphous structures for reaction-front reconstruction and the concomitant formation of disordered phases. Post-OER XPS analysis revealed an exceptionally high Mo leaching extent of up to 97.5% in a-NiMoO, resulting in the dynamic formation of V_M. Positron annihilation spectroscopy (PAS) was used to quantitatively probe defect characteristics, where the shortest lifetime component (τ_1) corresponded to small vacancies, while longer lifetimes signified clustered or extended vacancy defects.[162] The τ_1 value of d-NiOOH (187 ps) was significantly higher than that of *o*-NiOOH (156 ps), confirming higher concentration of Mo vacancies in the former (Fig. 10d). XAS analysis identified lower Debye–Waller factors (σ^2) for the Ni–O scattering path in NiOOH–C (0.0066 $Å^2$) reconstructed from amorphous NiO, compared with d-NiOOH (0.0078 $Å^2$), reflecting enhanced structural disorder in d-NiOOH arising from dynamic V_M generation. Benefiting from vacancy-induced disorder and electronic structure modulation, d-NiOOH achieved a current density of 100 mA cm^{-2} at an overpotential of only 201 mV, significantly outperforming NiOOH–C (297 mV). Mechanistically, vacancy-induced structural distortion strengthened Ni–O covalency and effectively activated O_L, driving the OER pathway from the conventional AEM toward LOM and thereby substantially improving overall kinetics. However, the intrinsic mechanism by which catalysts maintain long-term structural stability after the leaching of metal species and O_L has not been thoroughly investigated in this study.

Doping is generally regarded as an effective approach for optimizing intrinsic electronic structures by modulating lattice electron density and valence states.[165] The defect-inducing effect of doping arises from disparities in the valence state, ionic radius, electronegativity and coordination environment between dopant atoms and the host lattice. These mismatches require local lattice compensation, which in turn leads to structural distortion, vacancy formation, or the development of disordered regions. Liao *et al.*[32] introduced trace amounts of Ce into NiFe-LDH nanosheets to construct a NiFeCe-LDH@CP catalyst for the OER. Combined HRTEM, Raman and EPR analyses demonstrated pronounced Ce-doping-induced lattice distortion and disorder, accompanied by disruption of the layered framework and generation of dislocation defects (Fig. 10e). These structural perturbations not only increased the accessible surface area but also markedly enhanced surface V_O concentrations. DFT calculations further showed that the distortion-defect synergy optimized the local electronic structure of Ni sites and modulated intermediate adsorption energies, lowering the energy barrier of the rate-determining *OH → *O step from 2.3 eV to 1.66 eV (Fig. 10f). Beyond improving catalytic activity, achieving an optimal balance between activity and stability remained central to OER catalyst design. To this end, Shen *et al.*[166] introduced Al into high-entropy oxide (HEO) *via* molten-salt pyrolysis methods, named HEO-Al. V_O concentration in HEO-Al reached 32.75%, markedly higher than the 18.15% observed in undoped HEO, as determined by XPS (Fig. 10g and h). DFT results highlighted the critical role of moderate V_O concentrations in promoting OER deprotonation and strengthening O 2p-metal d orbital coupling, which effectively lowered the LOM energy barrier. Meanwhile, Al incorporation not only modulated defect formation but also increased the configurational entropy of the system, improving structural stability. This synergistic effect between defect engineering and high-entropy design enabled a dynamic balance between catalytic activity and durability by effectively suppressing structural degradation during electrolysis.

Heterointerface defects originate from interfacial structural and electronic mismatches, giving rise to local coordination distortion, electronic reconstruction, and defect accumulation, with pronounced implications for catalytic regulation.[167,168] Song *et al.*[169] constructed the $NiSe_2/FeSe_2$-NC nanoheterojunction enriched with interfacial structures and high-density vacancies *via* an *in situ* growth strategy, offering an ideal model system to elucidate interfacial regulation in the OER. Above 1.4 V, *in situ* XAS captured the development of pronounced Fe–M shells associated with *in situ*-formed Ni^{3+}–O–Fe^{3+} coordination motifs, identified as the genuine OER active centers (Fig. 10i). Notably, Se exhibited partial dissolution during operation, inducing transient Se-vacancy intermediates. Combined DFT and *operando* XAS analyses demonstrated pronounced weakening of local Fe–Se bonds by reaction-induced vacancy intermediates, which facilitated Fe oxidation to highly active (oxy)hydroxide species and lowered the energy barrier for active-phase formation. A comparison of Se vacancy formation energies indicated facile Se activation and dissolution in $NiSe_2$ (−1.69 eV), in contrast to the significantly higher vacancy formation energy in $FeSe_2$ (−0.38 eV) (Fig. 10j). Consequently, $NiSe_2/FeSe_2$ with moderate vacancy formation energy enabled dual regulation: controlled Se dissolution induced electronically favorable active vacancies at the interface, while excessive dissolution was suppressed to maintain overall structural integrity. In $NiSe_2/FeSe_2$-NC, dissolution-induced vacancies were stabilized by interfacial confinement, simultaneously improving conductivity, lowering the formation energy of the active phase, and preserving long-term structural integrity. Furthermore, the synergistic interplay among multiple types of defects enables multifaceted and precise modulation of electrocatalytic performance. Wang *et al.*[170] constructed the vacancy-rich CeO_2/Fe–$Co(OH)_2$ catalytic system.

DFT calculations demonstrated the thermodynamic spontaneity of Fe incorporation into $Co(OH)_2$ and further showed that Fe doping markedly lowered the V_O formation energy of $Co(OH)_2$. EPR results revealed substantially higher V_O concentrations in Fe–$Co(OH)_2$ than in pristine $Co(OH)_2$, with these concentrations being further amplified upon heterostructure formation with CeO_2. The introduction of additional V_O effectively activated O_L and promoted active phase (Co^{4+}–O_x) formation during the OER, thereby enhancing catalytic activity. However, to address the inherent activity–stability trade-off associated with excessive O_L participation, a dynamic interfacial electron backflow mechanism (CeO_2 → Co^{4+}–O_x) was established during the steady-state reaction. Owing to the higher work function of Co^{4+} (3.99 eV) relative to CeO_2 (2.92 eV), electrons were transferred from CeO_2 to the Co centers, partially reducing Co^{4+} to the more stable Co^{3+} state. This electron redistribution stabilized Co(IV)–O bonds and suppressed excessive O_L involvement, thereby mitigating over-oxidation-induced structural degradation (Fig. 10k). Meanwhile, interfacial bonding (*e.g.*, Ce–O–Co) effectively anchored V_O, suppressing their migration and aggregation at high potentials. Benefiting from these synergistic mechanisms, the catalyst maintained nearly unchanged V_O concentrations after continuous operation at 1000 mA cm^{-2} for 800 h, enabling long-term, high-current-density OER dominated by the LOM pathway.

6.1.2 Acidic OER. Relative to alkaline systems, the OER in acidic media encounters not only comparable intrinsic kinetic challenges but also a significantly more aggressive reaction environment. The strong corrosiveness of acidic electrolytes, coupled with pronounced electron dissipation under high anodic potentials, makes it difficult for surface active phases to maintain structural stability. Under such conditions, metal centers are prone to dissolution, migration, or excessive oxidation, which can ultimately trigger lattice collapse and irreversible structural reconstruction. As a result, achieving long-term stable operation under industrially relevant proton exchange membrane (PEM) conditions remains highly challenging.[171–173] In addition, the intrinsically high energy barriers of acidic OER render practical applications heavily dependent on noble-metal catalysts such as Ru-based materials, whose limited abundance, high cost, and structural instability under harsh operating conditions significantly hinder large-scale deployment.[174,175] Leveraging its unique advantages in tuning electronic structures, local coordination environments, and structural stability, the following section provides a systematic discussion of the roles and viable implementation strategies of common defects in acidic OER.

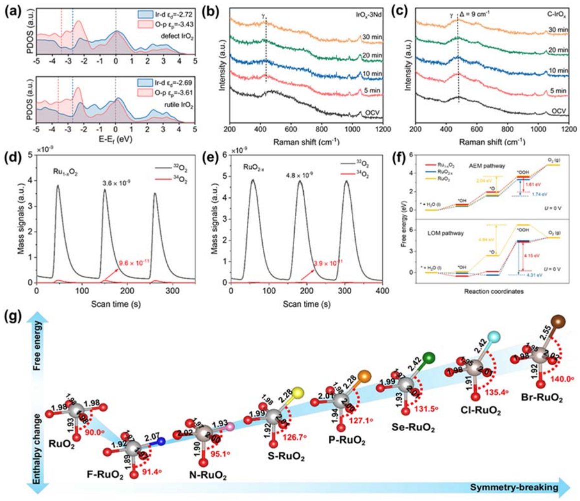

Fig. 11 (a) Density of states (DOS) plots of Nd leaching-induced defect IrO_2 and rutile IrO_2.[178] Copyright 2025 Wiley-VCH. (b and c) *In situ* Raman spectra of IrO_x-3Nd and C–IrO_x after 0–30 min OER tests.[178] Copyright 2025 Wiley-VCH. Differential electrochemical mass spectrometry (DEMS) signals of $^{16}O^{18}O$ and $^{18}O^{18}O$ from the OER products for ^{18}O-marked (d) $Ru_{1-x}O_2$ and (e) RuO_{2-x}.[179] Copyright 2024 American Chemical Society. (f) Free energy diagrams for AEM and LOM on the surfaces of $Ru_{1-x}O_2$, RuO_{2-x}, and RuO_2 under an electrode potential of 0 and 1.23 V.[179] Copyright 2024 American Chemical Society. (g) Reaction free energy and subsurface O loss enthalpy change volcano against the symmetry-breaking.[177] Copyright 2025 Springer Nature.

While LOM can markedly boost OER kinetics, it also triggers persistent O_L loss and metal dissolution, thereby undermining structural stability and accelerating catalyst deactivation.[176,177] Building on this concept, Zhang *et al.*[178] introduced rare-earth Nd during combined pyrolysis-acid leaching. Nd ion-coupled oxygen dissolution during acid treatment, followed by the subsequent leaching of Nd ions at the early reaction stage, triggered the generation of high-density and spatially controllable O_L vacancies. Meanwhile, the short-range quasi-crystalline rutile order was retained, ultimately leading to the formation of the IrO_x-3Nd catalyst. This structure provided abundant oxygen-unsaturated sites that facilitated intermediate adsorption and deprotonation, while simultaneously maintaining the integrity of the Ir–O–Ir network. Consequently, large-scale Ir–O bond cleavage and Ir ion dissolution under high potentials were effectively suppressed. DFT calculations demonstrated a defect-induced shift of the Fermi level in IrO_x-3Nd toward the O 2p band center (−3.43 eV), accompanied by a reduced energy gap between the Ir 5d and O 2p band centers (Fig. 11a), indicative of enhanced Ir–O covalency. This electronic modulation facilitated O_L activation by lowering the energy barrier for O_L oxidation, thereby promoting the LOM pathway and improving catalytic activity. To address the inherent activity–stability trade-off associated with LOM, the introduced V_O could be rapidly replenished by water molecules during catalysis, with a low energy barrier of only 0.42 eV. This dynamic vacancy refilling process enabled continuous O_L self-repair, preventing vacancy accumulation and suppressing structural degradation. *In situ* Raman spectroscopy indicated preferential adsorption of surface *OH species at vacancy sites, enabling reversible oxygen exchange processes that maintained the structural integrity of Ir–O bonds even under high anodic potentials (Fig. 11b and c). These findings highlighted a synergistic strategy in which defect-induced electronic structure modulation activated the LOM pathway, while dynamic oxygen replenishment and reversible intermediate adsorption collectively stabilized the catalyst structure, thereby achieving a balance between high catalytic activity and long-term stability.

Notably, redirecting the OER pathway serves as more straightforward strategy. As the classic electrocatalyst for acidic OER, the activity decay of RuO_2 mainly originates from structural instability induced by the LOM.[173] In this context, Pan *et al.*[179] systematically investigated the roles of cation- and anion-vacancy-modified RuO_2 catalysts ($Ru_{1-x}O_2$ and RuO_{2-x}) in acidic OER. As determined by *operando* DEMS, oxygen evolution on all catalysts was dominated by the formation of $^{32}O_2$, supporting an AEM-dominated OER pathway. Additionally, RuO_{2-x} produced only 0.56% $^{34}O_2$, compared with 3.4% for $Ru_{1-x}O_2$ and 7.2% for pristine RuO_2 (Fig. 11d and e). This behavior confirmed the stability of the AEM pathway and highlighted the role of defect engineering in suppressing the intrinsically unstable LOM. Meanwhile, the synergistic modulation of Ru and V_O optimized Ru–O bond strength and the electronic structure, reducing the energy barrier of the RDS from 2.04 eV to 1.61 eV and 1.74 eV, respectively (Fig. 11f). Accordingly, this approach achieved a synergistic balance between improved OER kinetic behavior and maintained structural stability. Moreover, Huang *et al.*[177] proposed a symmetry-breaking design strategy induced by anion doping for M–RuO_2 (M = F, S, Se, P, N, Cl, Br) on the basis of DFT calculations. Among these candidates, F-doped RuO_2 exhibited the lowest free energy barrier for the RDS (1.80 eV), highlighting its superior potential for achieving both high activity and enhanced stability in acidic OER (Fig. 11g). A higher maximum electron localization function (ELF) value was further observed for surface *OOH species on F–RuO_2 compared with pristine RuO_2, suggesting enhanced interaction strength between the *OOH intermediate and the catalyst surface. DOS analysis revealed effective modulation of the Ru d and O 2p electronic states upon F incorporation, accompanied by a downward shift of the O 2p band center from −2.96 eV to −3.23 eV. This downward shift increased the V_O formation energy, suppressing Ru dissolution and stabilizing O_L (Fig. 12a).

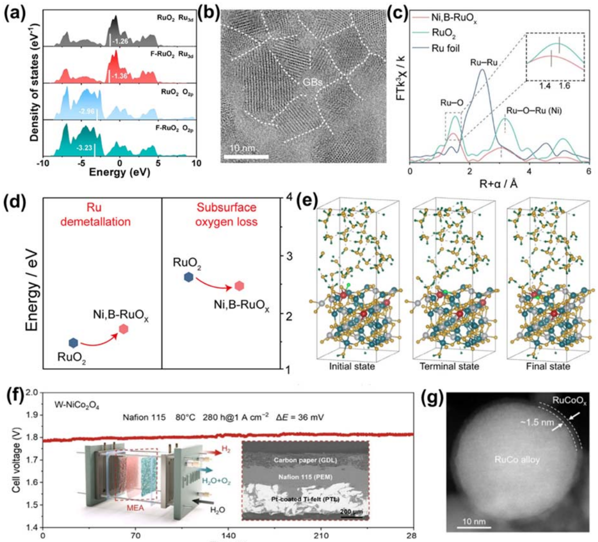

Fig. 12 (a) DOS of Ru 3d and O 2p for F–RuO_2 and RuO_2.[177] Copyright 2025 Springer Nature. (b) HRTEM image of Ni,B–RuO_x, with typical GBs regions highlighted by white dashed lines.[180] Copyright 2025 American Chemical Society. (c) Ru K-edge XAS spectra.[180] Copyright 2025 American Chemical Society. (d) Calculated energies for Ru structural degradation and surface oxygen loss in RuO_2 and Ni,B–RuO_x.[180] Copyright 2025 American Chemical Society. (e) *Ab initio* molecular dynamics (AIMD) snapshots of H_2O dissociation and *O migration into a lattice vacancy.[181] Copyright 2025 American Chemical Society. (f) Full-cell operation at 1 A cm^{-2} in pure water.[181] Copyright 2025 American Chemical Society. (g) High-angle annular dark-field scanning transmission electron microscopy (HAADF-STEM) image of the core/shell RuCo/$RuCoO_x$ nanospheres.[184] Copyright 2024 American Chemical Society.

In addition, both the enthalpy change associated with subsurface oxygen loss and the energy consumption required for Ru demetalation in F–RuO_2 were markedly higher than those in RuO_2, further confirming that symmetry breaking played critical roles in reinforcing lattice stability. Overall, the doping strategy simultaneously enhanced O-species adsorption and suppressed Ru demetalation, achieving synergistic improvement in catalytic activity and durability for acidic OER, while effectively shifting the reaction pathway from the LOM to the AEM. Considering that excessive suppression of the LOM pathway may lead to activity loss, Dai *et al.*[180] achieved cooperative regulation of LOM and AEM by co-doping Ni and B into RuO_2 *via* the solid–liquid reaction route. In this system, B doping induced the formation of GBs (Fig. 12b), significantly increasing the concentration of V_O and exposing more Ru active sites, while Ni preferentially accumulated near GBs under strain-driven effects, enabling synergistic structural modulation. XAS characterization revealed that Ni incorporation broke the symmetry of Ru–O octahedra and induced Ru–O bond contraction, thereby enhancing structural robustness (Fig. 12c).

DFT calculations further showed that GB regions exhibited a relatively low RDS barrier for the LOM pathway, whereas non-GB regions preferentially followed the AEM pathway with a barrier of 1.88 eV. This spatially resolved distribution of reaction pathways establishes a cooperative AEM-LOM mechanism between GBs and bulk regions. Importantly, to address the activity–stability trade-off associated with LOM-dominated systems, Ni and B co-doping significantly increased the Ru demetalation energy (Fig. 12d), effectively suppressing metal dissolution under acidic conditions. As a result, this system achieved the synergistic balance in which LOM-driven high activity at GBs regions was coupled with AEM-mediated stability in bulk regions.

The majority of existing studies focus on regulating the intrinsic activity of noble-metal-based catalysts, whereas the dynamic evolution of defects during catalysis has received far less attention, and noble-metal dependence remains persistently limiting. To address these limitations, Peng *et al.*[181] extended the investigation to non-precious metal systems (doping W into $NiFe_2O_4$) and proposed the dynamic oxygen replenishment mechanism (DORM) for the first time based on AEM and LOM. This strategy directly addressed the intrinsic instability of LOM, where O_L consumption often led to irreversible oxygen depletion and structural degradation. In this mechanism, O_L participating in O–O coupling could be continuously replenished by water-derived species (Fig. 12e). DFT calculations identified W–Co sites with lower water adsorption energy (−0.74 eV) and dissociation barriers (−0.63 eV), markedly promoting interfacial water activation and facilitating oxygen supply for O_L regeneration. As evidenced by structural characterization, the lattice distortion formation induced by W doping effectively lowered the surface protonation and vacancy formation energy, establishing a favorable structural foundation for O_L activation and dynamic replenishment. ELF analysis further revealed pronounced enhancement in the electronic polarization of Co–O bonds upon W incorporation, which promoted V_O healing and stabilized the O_L network. Meanwhile, AIMD simulations revealed that V_O induced by W doping could be rapidly filled by water dissociation products within approximately 360 fs, avoiding irreversible structural collapse caused by O_L depletion in conventional LOM pathways. Collectively, these results established a dynamic repair paradigm in which O_L activation and real-time oxygen replenishment are coupled, enabling sustained LOM activity while suppressing structural degradation. Benefiting from these advantages, W–$NiCo_2O_4$ achieved stable operation for 280 h at 1 A cm^{-2} in a PEM electrolyzer (Fig. 12f), providing a new design paradigm for non-precious-metal catalysts toward acidic OER. Regarding the activity–stability trade-off in the LOM-dominated OER, this work addresses the issue from multiple perspectives. First, appropriate defect engineering can modulate the d-band center to enhance M–O covalency and lower the energy barrier for O_L oxidation, thereby effectively activating the LOM pathway. The stability challenges of this mechanism have been addressed in previous work, where O_L replenishes depleted V_O through the DORM. In addition, electron back-donation can suppress over-oxidation of metal centers. Together, these effects mitigate structural degradation caused by O_L depletion, achieving a balance between efficient LOM activation and long-term structural stability. Furthermore, synergistic defect engineering strategies can construct spatially coupled AEM-LOM pathways while maintaining moderate LOM participation, thereby further reconciling catalytic activity and stability. These insights provide useful guidance for the rational design of high-performance OER catalysts.

On the basis of conventional regulation of vacancy and doping defects, heterointerfaces can endow materials with multilevel structural stability through interfacial bonding and synergistic effects of components.[182,183] Liu *et al.*[184] precisely controlled the oxidation conditions of RuCo alloy nanospheres to construct RuCo/$RuCoO_x$ core-shell heterostructures with tunable oxide-shell thicknesses. This structure was confirmed by HAADF-STEM characterization (Fig. 12g). GPA revealed a periodic distribution of maximum ε_{xx} strain at the interface, corresponding to dislocation-enriched regions that effectively exposed depletion-layer active sites and optimized the electronic structure. Computational simulations identified elongated Ru–O and Co–O bonds together with weakened covalency with increasing $RuCoO_x$ shell thickness, leading to energetically unfavorable O_L oxidation and improved structural stability.

6.1.3 Alkaline HER.

The HER is mechanistically regarded as relatively straightforward compared with the OER and is generally described by the Volmer–Heyrovsky or Volmer–Tafel pathways. Nevertheless, HER activity is simultaneously constrained by several factors in practical electrode systems, including the intrinsically high energy barrier for water dissociation, limited proton/electron transport, non-optimal ΔG_{H^*} and poisoning of active sites.[185] In recent years, defect engineering has been extensively employed to address these limitations and has demonstrated remarkable potential for catalytic performance optimization.

Layered MoS_2, the prototypical HER catalyst, serves as the representative example in which V_S are widely recognized as key

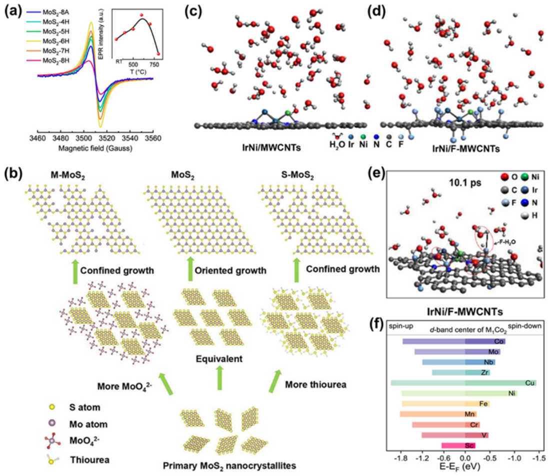

Fig. 13 (a) EPR spectra of the different defected MoS_2.[68] Copyright 2019 American Chemical Society. (b) Schematic diagram of the synthesis of different vacancy states MoS_2 by controlling the ratio of sulfur to molybdenum in the reactants.[187] Copyright 2024 American Chemical Society. Atomic configurations of an equilibrated (c) H_2O–IrNi/F-MWCNTs interface and (d) H_2O–IrNi/MWCNTs interface in alkaline media.[188] Copyright 2025 Wiley-VCH. (e) Atomic configuration of an equilibrated H_2O–IrNi/F-MWCNTs interface at ≈10.1 ps in alkaline media.[188] Copyright 2025 Wiley-VCH. (f) The calculated d-band center for spin-up and spin-down.[191] Copyright 2025 Wiley-VCH.

active motifs that activate otherwise inert basal planes and expose edge-like active sites, enhancing HER activity.[186] Li *et al.*[68] introduced V_S into MoS_2 nanosheets *via* H_2 annealing at temperatures ranging from 400 to 800 °C. As evidenced by EPR measurements, the V_S concentration exhibited nonmonotonic dependence on temperature, increasing initially to the maximum at 600 °C and decreasing upon further heating. This behavior originated from the formation of isolated point defects at relatively low temperatures, which generated Mo–S dangling bonds, whereas progressive sulfur stripping leaded to the formation of extended defect regions at higher temperatures, reducing the number of Mo–S dangling bonds and thus weakening the EPR signal (Fig. 13a). Electrochemical measurements demonstrated that such vacancy defects significantly enhanced HER activity. To further elucidate the influence of the local vacancy environment on catalytic performance, Zhou *et al.*[187] employed the confined growth strategy, in which excessive adsorption of reactant molecules on nascent nanocrystal surfaces during hydrothermal synthesis inhibited continuous oriented growth, yielding MoS_2 samples enriched with vacancy defects. Modulating the Mo/S ratio allowed the formation of vacancies with distinct atomic environments (S–MoO_2 and M–MoO_2, Fig. 13b), enabling the construction of seven Mo/S ratios and sixteen vacancy models with different local coordination structures. Consistent experimental observations and DFT calculations identified M–MoO_2 vacancies, characterized by higher density of terminal Mo atoms, as exhibiting more favorable hydrogen adsorption and delivering optimal HER activity. Further analysis highlighted the critical role of the local atomic configuration around vacancies in tuning the surface electronic structure and orbital distribution, enabling near-thermodynamically optimal Mo–H interactions and balanced *H adsorption–desorption behavior.

Besides vacancy defects, doping defects have also been widely employed to optimize the catalytic performance of alkaline HER systems. Zong *et al.*[188] synthesized F-doped multiwalled carbon nanotubes loaded with IrNi nanoclusters using a high-temperature ultrafast shock process (1200 °C for 10 s) under vacuum. AIMD simulations identified hydrogen-bond interactions between F dopants and interfacial water molecules, which guided water molecules toward the catalyst surface and promoted an ordered interfacial water structure. This reorganization shortened the average water-surface distance from 5.35 to 5.05 Å, strengthening interfacial adsorption (Fig. 13c and d). *Operando* attenuated total reflection-surface-enhanced infrared absorption spectroscopy (ATR-SEIRAS) measurements revealed a pronounced red shift and intensity enhancement of the ν-OH vibration, further confirming the optimized alignment of interfacial water molecules. On the IrNi/F-MWCNTs surface, metadynamics simulations captured H–O bond dissociation of water molecules within 10.1 ps, in sharp contrast to the undoped counterpart where no dissociation was observed, thereby evidencing a markedly lowered water dissociation barrier for the Volmer step upon F doping (Fig. 13e). When assembled into an anion exchange membrane water electrolyzer (AEMWE), this catalyst delivered an industrially relevant current density of 1 A cm^{-2} at 1.82 V, highlighting its promising application potential. In addition, cobalt phosphide (Co_2P), owing to its near-optimal hydrogen binding energy (HBE) under alkaline conditions, had been extensively investigated as a HER catalyst.[189,190] Yuan *et al.*[191] systematically introduced transition-metal dopants into Co_2P to construct a series of metal-doped Co_2P nanocomposite frameworks (M-CPNCF), aiming to elucidate the role of secondary transition metals in Co_2P. Metal centers with distinct coordination environments enabled precise modulation of the d-orbitals due to their differences in d-band filling and spin polarization, thereby effectively tuning the adsorption energies of reaction intermediates (Fig. 13f). Specifically, active sites with lower d-band filling possessed higher d-orbital energy levels and a greater number of unoccupied orbitals, which facilitated electron transfer from these unoccupied states to bonding orbitals, thereby strengthening adsorption interactions.[192] From a spin-polarization perspective, the elevation of antibonding states in spin-down d orbitals enhanced bonding interactions, whereas the lowering of antibonding states in spin-up d orbitals weakened bonding strength, and the competition between these effects ultimately determined the adsorption energy.[193] Combined theoretical and experimental results identified Fe doping as the most effective strategy to synergistically regulate water dissociation kinetics, OH binding energy, and *H adsorption–desorption behavior at Co active sites, leading to thermodynamically favorable conditions and enhanced HER activity.

Heterointerface defects represent another effective strategy for enhancing catalytic performance toward the alkaline HER. Structural mismatch at heterointerfaces frequently induces vacancies and strain, which act as key electronic modulation sites. These defect-rich interfaces generate localized polarized electric fields, facilitate charge redistribution, and cooperatively optimize the adsorption/desorption energetics of water and reaction intermediates, thereby overcoming the limitations of single-phase catalysts.[194,195] Zhang *et al.*[72] prepared IrNi nanoclusters at 300 °C and constructed a Mo_2N/MoO_3@NC-30 heterojunction by exploiting lattice mismatch to induce interfacial vacancies. Experimental and theoretical results collectively identified interfacial vacancies as key contributors to enhanced interfacial polarization and stabilization of high-valence Mo species in the vicinity of N sites. Such electronic regulation suppressed *OH adsorption while favoring *H desorption to H_2, ultimately boosting catalytic activity. Moreover, the "spillover effect" induced by heterointerfaces optimized intermediate coverage, maintained an optimal adsorption balance, and suppressed active-site poisoning, providing an intrinsic driving force for HER enhancement.[196,197] Zhang *et al.*[197] anchored Ru clusters onto Mn_3O_4 *via* Ru–O–Mn linkages to construct an Ru@Mn_3O_4 heterostructure with compressive strain. Compared with Mn_3O_4 obtained by simple physical mixing without compressive strain, this structure exhibited superior HER catalytic performance. In Ru and Mn_3O_4 single-component systems, *in situ* Raman spectra showed progressively intensified M–O (M = Ru, Mn) vibrations with increasing potential, reflecting sustained water dissociation and the accumulation of surface OH species. In contrast, the

OH adsorption signal weakened with increasing potential for Ru@Mn_3O_4 with compressive strain, suggesting that the heterointerface provided an efficient OH desorption pathway (Fig. 14a). According to DFT analysis, Mn_3O_4 favored water dissociation owing to its high oxophilicity, while Ru–O–Mn interfacial sites with weaker OH binding acted as desorption channels for accumulated OH species, enabling efficient OH spillover (Fig. 14b). This offered a new insight into optimizing the HER. More intriguingly, beyond the deliberate construction of heterojunctions, catalysts may also undergo *in situ* structural reconstruction under electrochemical operating conditions, spontaneously generating new heterointerfaces. Wang *et al.*[198] tracked the dynamic surface evolution of $BaRuO_3$ (BRO) by TEM, showing a transition from an initially smooth surface to a stabilized Ru/$BaRuO_3$ heterostructure during operation. Nanoscale clusters appeared within 127 s, evolved into metallic Ru domains with clear lattice fringes by 453 s and eventually stabilized as *in situ* exsolved Ru nanoparticles at longer times (918–1458 s), accompanied by abundant V_O (Fig. 14c), which resulted in significantly enhanced HER performance. This study demonstrated that the synergistic interplay between *in situ* reconstruction and defect generation could substantially improve the intrinsic catalytic properties, offering an important design paradigm for alkaline HER catalysts.

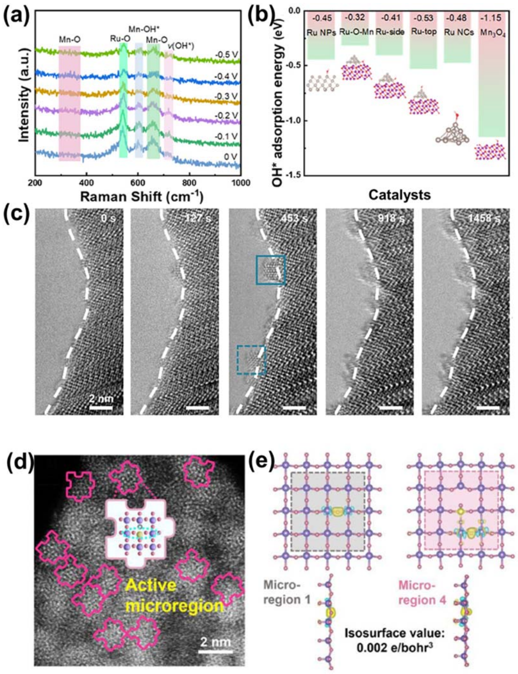

Fig. 14 (a) *In situ* Raman spectra of Ru@Mn_3O_4.[197] Copyright 2025 Wiley-VCH. (b) *OH adsorption energies on Ru NPs, Ru–O–Mn sites, Ru-side, Ru-top, Ru NCs, and Mn_3O_4.[197] Copyright 2025 Wiley-VCH. (c) HRTEM images of initial BRO showing *in situ* Ru exsolution over time under TEM observation (time indicated in seconds).[198] Copyright 2025 American Chemical Society. (d) Annular correlative HAADF-STEM (AC HAADF-STEM, the jigsaw in the figure is the active micro-region).[199] Copyright 2025 Wiley-VCH. (e) Front and side views of differential charge density for the optimal O sites in different micro-regions.[199] Copyright 2025 Wiley-VCH.

6.1.4 Acidic HER. In strongly acidic environments, the HER generally exhibits intrinsically fast kinetics. Nevertheless, multiple challenges remain in practical electrocatalytic systems. First, most non-noble-metal catalysts suffer from low charge-transfer efficiency and non-optimal hydrogen adsorption energies in acidic media, leading to sluggish reaction kinetics.[200,201] More critically, the aggressive corrosiveness of strong acids severely compromises metal-coordination frameworks. At high potentials and large current densities, catalysts are prone to metal dissolution, structural reconstruction, or destabilization of surface oxides, which substantially limits their long-term operational stability.[200,202,203] To address these issues, defect engineering has recently emerged as an effective strategy to modulate local structures and electronic states, thereby enhancing both the activity and durability of acidic HER catalysts.

Defects can effectively break local coordination symmetry and regulate metal–hydrogen interactions, driving the ΔG_{H^*} toward the thermodynamically optimal region. Zhao *et al.* and Tsai *et al.*[204,205] introduced controllable V_S into the basal plane of MoS_2. According to DFT analysis, the approach of ΔG_{H^*} toward thermoneutrality at vacancy-adjacent sites enabled the catalytic activation of the intrinsically inert basal plane. Building on this concept, Han *et al.*[206] employed $NiPS_3$ as the model system to systematically investigate the effects of neighboring Ni vacancies (V_{Ni}) and V_S on water adsorption/dissociation and the electrochemical adsorption behavior of generated protons on the catalyst surface. With further removal of Ni atoms adjacent to V_S, water molecules underwent self-orientation, enabling H atoms to form hydrogen bonds with neighboring S atoms and thereby stabilizing molecular physisorption. Meanwhile, the synergistic introduction of dual vacancies dramatically reduced the water dissociation energy from 0.88 eV to −0.91 eV. In this process, water molecules adsorbed at V_S sites in a "pseudo-substitutional" manner, followed by dissociation, with the resulting OH and H species occupying V_S and V_{Ni}, respectively. The resulting Ni–S dual-vacancy structure exhibited ΔG_{H^*} (−0.09 eV) close to the ideal value, leading to an overall enhancement in HER activity. It is worth noting that these studies are primarily based on static structural and energetic analyses. Direct experimental evidence for capturing the real-time occupation, release and dynamic evolution of vacancies during catalysis remains scarce and represents a critical challenge for future investigations.

In addition, Zheng *et al.*[199] constructed a porous layered MoO_{3-x}/Mo_2AlB_2 structure *via* an alkaline hydrothermal etching-intercalant intercalation synergistic strategy. The resulting material was subsequently mixed with ruthenium chloride ($RuCl_3$) and treated *via* ultrafast Joule heating to obtain Ru–MoO_{3-x}/Mo_2AlB_2 composite catalysts. As evidenced by EPR and XAS analyses, the introduction of abundant V_O and lattice distortions within molybdenum oxide layers could be attributed to the synergistic action of etching and doping. These defect-rich regions promoted the formation of active microdomains, in which Ru atoms and V_O were preferentially enriched and acted as the dominant catalytically active centers (verified by AC

HAADF-STEM characterization, Fig. 14d). AIMD analysis of the active microdomains showed preferential stabilization of Ru atoms at sites adjacent to V_O, corresponding to the most thermodynamically favorable configurations. Further analysis revealed that within the microdomains, the ΔG_{H*} values of Mo and Ru sites were significantly higher than those of O atoms adjacent to Ru–O_v–Mo motifs, whereas the latter exhibited ΔG_{H*} values close to zero, indicating that electron-rich oxygen sites served as the primary HER active centers (Fig. 14e). This finding challenged the conventional paradigm of metal-centered activity, demonstrating that the cooperative formation of V_O and Ru doping induced electron accumulation on oxygen sites, rendering them highly efficient hydrogen evolution centers. Moreover, coupling the layered conductive support with low-crystallinity active phases endowed the system with both high structural stability and electron-unsaturated metal dangling bonds characteristic of amorphous materials, thereby markedly enhancing HER activity. Benefitting from these structural and electronic modulations, the catalyst delivered a current density of 10 mA cm^{-2} at an overpotential of only 38 mV in acidic media and exhibited excellent long-term stability.

6.2 Complex water electrolysis systems

With the continuous advancement of research, water electrolysis systems have gradually evolved from conventional acidic and alkaline electrolytes with simple compositions to more complex aqueous environments.[207] Among these, seawater electrolysis, as the representative complex system, has emerged as a prominent research focus in the field of renewable energy. Currently, seawater electrolysis research has primarily emphasized alkaline and neutral-media electrolysis systems. While the preceding sections mainly discussed the role of defect engineering in regulating electronic configurations, intermediate adsorption, and reaction pathways for the HER/OER in freshwater systems, the complex ionic environment inherent to seawater electrolysis exerts a much more complicated influence on catalytic activity and structural stability (Fig. 15). On the anodic side of seawater electrolysis, high concentrations of Cl^- exhibit pronounced thermodynamic and kinetic competition with the OER.[208,209] On the one hand, chloride oxidation can proceed in parallel with the OER, significantly compromising reaction selectivity. On the other hand, Cl^- and its oxidative derivatives are highly corrosive toward anode materials, readily inducing metal dissolution, lattice degradation and active-site passivation,[210,211] thereby accelerating catalyst deactivation. Simultaneously, on the cathodic side, water reduction ($H_2O \rightarrow H_2 + OH^-$) leads to a sharp local increase in pH, providing direct thermodynamic driving force for the precipitation of Ca^{2+} and Mg^{2+} as hydroxides. The resulting $Mg(OH)_2/Ca(OH)_2$ deposits severely impede charge transfer and mass transport, representing another dominant degradation pathway in seawater electrolysis. The following section systematically summarizes the regulation strategies and underlying mechanisms of defect engineering in addressing the typical challenges of seawater electrolysis (Fig. 15).

To mitigate anodic Cl^- corrosion, current strategies primarily rely on the construction of dense oxide protective layers or the incorporation of polyanionic species with inherent Cl^--repelling capability.[212,213] While these approaches can partially suppress chloride-induced degradation, dense protective layers often impede access to OER active sites. Meanwhile, polyanionic species tend to suffer from gradual depletion at industrially relevant current densities owing to intense gas evolution and electrolyte convection, ultimately compromising catalytic activity and long-term stability.[214,215] To overcome these limitations, Li *et al.*[216] proposed an alternative interface design strategy distinct from the conventional "coating-isolation" paradigm. By epitaxially depositing catalytic nanoparticles onto heterophase nanorods, the NiTe/Ni_2FeP heterojunction catalyst was constructed, which intrinsically avoided physical blockage of active sites and enabled both high activity and durability for direct seawater electrolysis. The abundant interfacial regions in

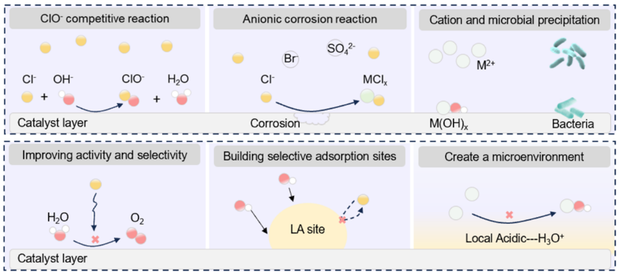

Fig. 15 Schematic illustration of the main challenges and corresponding mitigation strategies in seawater electrolysis.

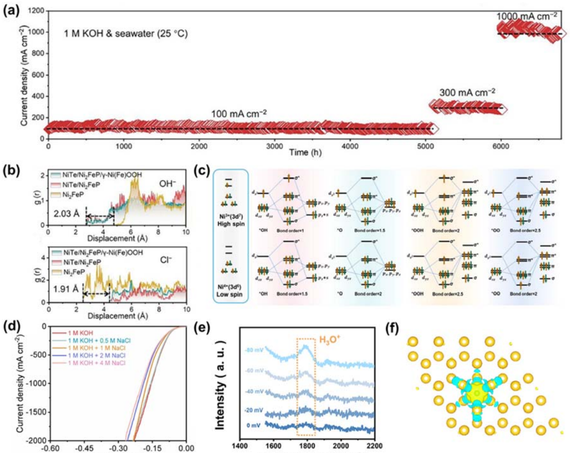

Fig. 16 (a) Long-term durability test of NiTe/Ni_2FeP/NF in 1 M KOH + seawater measured at 1.6, 1.8, and 2.2 V *vs.* RHE, corresponding to current densities of 100, 300, and 1000 mA cm^{-2}, respectively.[216] Copyright 2026 Wiley-VCH. (b) OH^- and Cl^- concentrations at positions (distance) perpendicular to Ni_2FeP and NiTe/Ni_2FeP.[216] Copyright 2026 Wiley-VCH. (c) Schematic illustration of orbital hybridization between Ni and reaction intermediates under Ni^{3+} and Ni^{4+}.[218] Copyright 2025 Wiley-VCH. (d) Linear sweep voltammetry (LSV) curves and overpotentials of Ru/V–NiO in simulated seawater with varying NaCl concentrations.[219] Copyright 2025 Elsevier B.V. (e) *In situ* Raman spectra in natural seawater of B–Os at differing potentials.[220] Copyright 2025 Wiley-VCH. (f) The DCD of B–Os.[220] Copyright 2025 Wiley-VCH.

this architecture induced a built-in electric field (BEF). Molecular dynamics simulations revealed that the BEF, in synergy with the applied electric field, enhanced interfacial enrichment and adsorption of OH^- while effectively suppressing competitive Cl^- dsorption, thereby markedly improving OER selectivity. As a result, this catalyst exhibited stable operation for over 6800 h at industrial current densities, demonstrating outstanding activity and structural robustness (Fig. 16a and b). Moreover, hard acidic metal sites preferentially adsorbed OH^- during anion competition processes according to the hard–soft acid–base (HSAB) theory.[217] Building on this principle, Wang *et al.*[218] introduced V_O into Fe-doped nickel hydroxide (Ni^{II}–Fe) with an area of approximately 2000 cm^{-2} *via* two-step impregnation synthesis. Experimental and theoretical analyses revealed the "maturation" mechanism of V_O that significantly promoted the formation of high-valence Ni^{4+} species, thereby enhancing the hard-acid character of Ni sites. Specifically, V_O regulated local charge redistribution, reduced proton desorption energy and tuned the antibonding orbitals of Ni–O bonds, narrowing the bandgap and substantially lowering the energy barriers for the $Ni^{2+} \rightarrow Ni^{3+} \rightarrow Ni^{4+}$ oxidation transitions (Fig. 16c). The enrichment of OH^- species near vacancy-rich catalysts was supported by AIMD simulations, with a concentration of 4.4 M at 6 Å above the electrode surface compared to 1.3 M for vacancy-free samples. In contrast, the Cl^- concentration at 14 Å is reduced to ∼45% of that in the control. These results collectively highlighted the exceptional Cl^- corrosion resistance and high OER selectivity of V_O-engineered NiFe catalysts. When applied in AEMWE, the catalyst delivered an operating voltage of only 1.68 V at 0.5 A cm^{-2}, achieving hydrogen production cost lower than 50% of the U.S. DOE's 2026 target, thereby demonstrating promising scalability and practical application potential.

In addition to anodic chloride corrosion, Ca^{2+}/Mg^{2+} precipitation at the cathode represents another critical challenge in seawater electrolysis, originating from cathode-induced local alkalization that thermodynamically drives hydroxide formation. Liu *et al.*[219] synthesized an Ru/V–NiO heterostructure composed of Ru nanoparticles supported on vanadium-doped nickel oxide *via* hydrothermal treatment followed by N_2 annealing. The reduction in the water dissociation energy barrier, together with weakened Cl^- adsorption at active sites, as supported by *in situ* Raman and DFT analyses, could be attributed to the synergistic effects of Ru/V–NiO interfacial construction and V_O introduction. Consequently, the catalytic performance remained nearly unchanged even at elevated chloride concentrations, endowing the material with excellent resistance to seawater corrosion (Fig. 16d). Furthermore, Fu *et al.*[220] rapidly synthesized interstitial boron-doped osmium (B–Os) catalysts using the microwave-assisted quasi-solid-state method, enabling precise regulation of the interfacial microenvironment. TEM- and GPA-based strain analysis demonstrated the coexistence of compressive and shear strains in the lattice, leading to lattice distortion and local atomic disorder that facilitate the exposure of catalytically active sites. *In situ* Raman results highlighted the role of B–Os in creating a locally acidic interfacial environment that mitigated OH^- coprecipitation with Ca^{2+}/Mg^{2+} during the HER (Fig. 16e). Differential charge density (DCD) analysis further indicated that interstitial boron triggers electron accumulation and the formation of negatively charged centers at Os sites (Fig. 16f). The resulting electronic structure not only electrostatically suppressed Cl^- corrosion but also promoted preferential H_3O^+ adsorption, thereby achieving simultaneous resistance to corrosion and precipitation. When paired with a RuO_2 anode in an AEM electrolyzer, the system operated in natural seawater at 1 A cm^{-2} with a cell voltage of only 1.73 V and maintained stable performance for over 400 h. In summary, defect engineering not only substantially enhances the intrinsic HER/OER activity in seawater systems but also strengthens electrodes against precipitation, chloride corrosion and interfacial mass-transport limitations through multidimensional regulation of interfacial electronic structures and reaction microenvironments. As such, it has emerged as the core design paradigm for the development of efficient and durable seawater electrolysis systems.

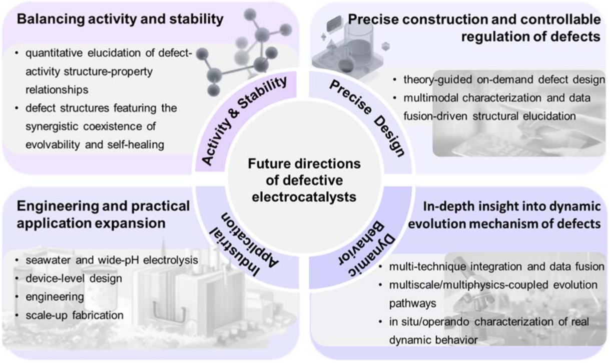

Fig. 17 Future development directions of defect-engineered electrocatalysts.

7 Conclusions and perspectives

This review focuses on the structural regulation effects and structure–activity relationships of defect engineering in electrocatalytic systems, and provides a systematic survey and critical analysis of recent advances in water electrolysis-related electrocatalysis. The main contributions of this review can be summarized as follows. First, from the perspectives of structural hierarchy and chemical nature, various types of defects in electrocatalytic materials are systematically classified. The common characteristics and distinct roles of different defects in regulating local coordination environments, electronic structures, and interfacial reaction properties are comparatively analyzed, thereby establishing a unified structural framework for understanding defect-performance relationships. Second, the characteristics of chemical and physical synthesis strategies in controlling defect type, concentration, and structural stability are comprehensively summarized, highlighting the critical influence of synthesis pathways on the controllability of defect construction. Furthermore, particular emphasis is placed on the dynamic evolution behavior of defects. By integrating recent advances in *in situ* and *operando* characterization techniques, this review elucidates the intrinsic nature of defect reconstruction during material synthesis, activation, and electrocatalytic operation, underscoring the decisive importance of working-state structures over static characterization in establishing reliable structure–activity correlations. The significance of this dynamic investigation lies in two aspects: (1) it reveals the pronounced "non-static" nature of defects in electrocatalytic systems, challenging the conventional view of defects as fixed structural entities and demonstrating that they undergo continuous dynamic evolution, including-formation or self-healing, migration or aggregation, and reconstruction, under multiple external stimuli. This advances the research paradigm from static structural characterization toward dynamic mechanistic understanding. (2) It establishes a structure–activity relationship framework based on "*operando* defect dynamics", overcoming the limitations of *ex situ* characterization in capturing real active sites and reaction pathways. By integrating *in situ*/*operando* techniques with the dynamic evolution of defects, it elucidates that catalytic performance originates from dynamic equilibrium of defect structures during the reaction, thereby providing a more reliable theoretical foundation for elucidating electrocatalytic mechanisms. Finally, the regulatory roles of defects in water electrolysis reactions are systematically summarized. The critical functions of defects in providing low-coordination active sites, modulating intermediate adsorption behavior, and facilitating key reaction pathways are clarified, further highlighting the essential role of defect engineering in overcoming the intrinsic performance limitations of conventional water-splitting electrocatalysts.

Despite the significant progress achieved, defect engineering in water-electrolysis electrocatalysis still faces several fundamental scientific challenges and practical bottlenecks that require further breakthroughs. First, regarding precise defect construction and controllable regulation, existing strategies still lack sufficient capability for independent control of defect type, spatial distribution, and concentration at the atomic scale. To address this limitation, future research should adopt a thermodynamics-kinetics co-regulation framework, in which defect formation energy landscapes are tuned *via* precursor chemistry, reaction temperature, electrochemical potential, and strain engineering. In parallel, predictive theoretical approaches should be employed to pre-evaluate defect stability and guide application-oriented defect design, enabling truly "on-demand" construction of defect structures. Moreover strengthening multimodal characterization integration and data fusion to establish an integrated framework linking defect evolution, electronic structure, and reaction kinetics. These approaches enable precise tuning of defect density, distribution, and local coordination environments in a controllable manner. Second, the causal relationship between defect dynamic evolution and catalytic performance is yet to be fully elucidated. Although *in situ* techniques can capture certain aspects of defect evolution, the true evolution pathways of defects under multiscale and multiphysical-field coupling conditions remain poorly understood. Strengthening multimodal characterization and data integration is therefore essential to establish a unified framework linking defect evolution, electronic structure, and reaction kinetics. Third, achieving a balance between high catalytic activity and long-term stability remains a central challenge for defect-rich catalysts in practical applications. Excessive defect density may significantly enhance initial activity but can also induce structural collapse, uncontrolled phase transitions, or metal dissolution. Designing defect architectures that are "evolvable yet structurally stable" through heterointerface engineering, synergistic doping, or dynamic self-repair mechanisms, represents a key future direction. Finally, from an application perspective, the adaptability of defect-engineered catalysts under seawater electrolysis, wide-pH conditions, and at industrial-level high current densities still requires systematic evaluation. Integrating defect-engineering concepts with device-level design, reaction engineering, and scalable manufacturing processes is essential for translating laboratory-scale advances into practical energy-conversion technologies. Overall, with the continued advancement of *in situ* characterization techniques, theoretical modeling, and materials synthesis, defect engineering is expected to evolve from empirical regulation toward rational and predictive design, playing an increasingly central role in the development of efficient, stable, and sustainable electrocatalytic systems for water electrolysis (Fig. 17).

Author contributions

Xaiojun Wang and Zexing Wu wrote and edited the original draft. All authors contributed to the figures, review, and editing of the manuscript.

Conflicts of interest

There are no conflicts to declare.

Data availability

No primary research results or new data were generated or analysed as part of this review.

Acknowledgements

The authors are thankful for funding support from the National Natural Science Foundation of China (52371227; 22278175), Taishan Scholar Young Talent Program (tsqn202408200), Shandong Province "Double-Hundred Talent Plan" (WST2020003), Zhejiang Provincial Natural Science Foundation of China (Grant No. LZ24B060001), and State Key Laboratory of New Textile Materials and Advanced Processing, Wuhan Textile University (FZ 2025022).

References

1 Y. Zhang, D. Gong, X. Yang, H. Qu, Z. Tong, X. Meng and K. Huang, *Environ. Chem. Saf.*, 2025, **1**(2), 9600033–9603940.
2 Q.-L. Hong, X. Xiao, X. Ai, H. Liu, G.-R. Xu, Q. Xue, X. Wang, B. Y. Xia and Y. Chen, *Chem. Soc. Rev.*, 2025, **54**, 9849–9875.

3 W. Song, J. Wu, J. Li, Z. Wang, T. He, W. Chen, D. Sun and J. Wu, *Green Carbon*, 2024, **2**, 393–400.

4 J. Gao, S. C. S. Shiong and Y. Liu, *Chem. Eng. J.*, 2023, **472**, 145033.

5 Q. Zhang, Y. Li, F. Luo and Z. Yang, *Chem. Commun.*, 2025, **61**, 10747–10763.

6 R. Deng, M. Guo, C. Wang and Q. Zhang, *Nano Mater. Sci.*, 2024, **6**, 139–173.

7 Y. Lu, L. Zhou, S. Wang and Y. Zou, *Nano Res.*, 2023, **16**, 1890–1912.

8 Y. Zhang, J. Liu, Y. Xu, C. Xie, S. Wang and X. Yao, *Chem. Soc. Rev.*, 2024, **53**, 10620–10659.

9 Y. Wang, P. Han, X. Lv, L. Zhang and G. Zheng, *Joule*, 2018, **2**, 2551–2582.

10 H. Arandiyan, S. S. Mofarah, Y. Wang, C. Cazorla, D. Jampaiah, M. Garbrecht, K. Wilson, A. F. Lee, C. Zhao and T. Maschmeyer, *Chem.–Eur. J.*, 2021, **27**, 14418–14426.

11 X. Zheng, S. S. Mofarah, C. Cazorla, R. Daiyan, A. A. Esmailpour, J. Scott, Y. Yao, S. Lim, V. Wong, E. Y. Chen, H. Arandiyan, P. Koshy and C. C. Sorrell, *Adv. Funct. Mater.*, 2021, **31**, 2103171.

12 D. Hao, J. Ren, Y. Wang, H. Arandiyan, M. Garbrecht, X. Bai, H. K. Shon, W. Wei and B.-J. Ni, *Adv. Energy Mater.*, 2021, **2021**, 12.

13 X. Geng, M. Vega-Paredes, Z. Wang, C. Ophus, P. Lu, Y. Ma, S. Zhang, C. Scheu, C. H. Liebscher and B. Gault, *Nat. Commun.*, 2024, **15**, 8534.

14 Y. Zhang, H. Liu, S. Zhao, C. Xie, Z. Huang and S. Wang, *Adv. Mater.*, 2023, **35**, 2209680.

15 M. Zhang, B. Zhou, L. Guo, H. Li, W. Xiao, G. Xu, D. Chen, C. Li, Y. Du, Z. Wu and L. Wang, *Inorg. Chem. Front.*, 2024, **11**, 5884–5893.

16 T. Wu, C. Dong, D. Sun and F. Huang, *Nanoscale*, 2021, **13**, 1581–1595.

17 X. Zhou, T. Yang, T. Li, Y. Zi, S. Zhang, L. Yang, Y. Liu, J. Yang and J. Tang, *Nano Res. Energy*, 2023, **2**, e9120086.

18 J. Li, R. Guo, X. Zang, Y. Wang, H. Li, W. Xiao, L. Xin, Y. Zong, G. Fu, Z. Wu and L. Wang, *Inorg. Chem. Front.*, 2025, **12**, 821–832.

19 B. Sun, W. Zhong, H. Liu, X. Ai, S. Han and Y. Chen, *EnergyChem*, 2025, **7**, 100148.

20 Z.-H. Yuan, T.-J. Wang, B. Sun, Q.-L. Hong, X. Ai, S.-N. Li, J. Bai and Y. Chen, *Appl. Catal., B*, 2025, **366**, 125041.

21 J. X. Zheng, D. P. Meng, J. X. Guo, X. B. Liu, L. Zhou and Z. Wang, *Adv. Mater.*, 2024, **36**, 2405129.

22 Y. Q. Chen, X. Y. Li and P. F. Ou, *Front. Energy*, 2025, **19**, 59–68.

23 H. Y. Zhang, L. L. Wu, R. H. Feng, S. H. Wang, C. S. Hsu, Y. M. Ni, A. Ahmad, C. R. Zhang, H. F. Wu, H. M. Chen, W. Zhang, Y. Li, P. Liu and F. Song, *ACS Catal.*, 2023, **13**, 6000–6012.

24 Z. Z. Liu, T. Liu, Q. N. Lin, C. Y. Bao and L. Y. Zhu, *Angew. Chem., Int. Ed.*, 2015, **54**, 174–178.

25 V. H. Hoa, S. Sidra, H. T. Dao, M. Mai, V. Rajendiran, S. W. Han and D. W. Kim, *Appl. Catal., B*, 2026, **380**, 125800.

26 M. Zhou, Y. Zhao, Z. W. Liu, X. R. Zhao, E. Z. Liu, L. Y. Xiao, P. F. Yin, C. K. Dong, H. Liu, X. W. Du and J. Yang, *Nano Res.*, 2024, **17**, 4711–4719.

27 Y. J. Liu, Y. B. Xu, Y. Tian, S. Guo, H. F. Li, X. Y. Yuan, Z. J. Zhao, B. C. Xu, X. J. Wang, P. Wang and Z. M. Liu, *ACS Catal.*, 2025, **15**, 3378–3390.

28 X. Zhong, E. X. Yuan, F. Yang, Y. Liu, H. Lu, J. Yang, F. Gao, Y. Zhou, J. M. Pan, J. W. Zhu, C. Yu, C. Z. Zhu, A. H. Yuan and E. H. Ang, *Proc. Natl. Acad. Sci. U. S. A.*, 2023, **120**, e2306673120.

29 R. Jiang, Y. M. Da, J. F. Zhang, H. Wu, B. B. Fan, J. H. Li, J. J. Wang, Y. D. Deng, X. P. Han and W. B. Hu, *Appl. Catal., B*, 2022, **316**, 121682.

30 Y. Wang, H. Arandiyan, S. S. Mofarah, X. J. Shen, S. A. Bartlett, P. Koshy, C. C. Sorrell, H. Y. Sun, C. Pozo-Gonzalo, K. Dastafkan, S. Britto, S. K. Bhargava and C. Zhao, *Adv. Mater.*, 2024, **36**, 2402156.

31 J. H. Yang, L. L. An, S. Wang, C. H. Zhang, G. Y. Luo, Y. Q. Chen, H. Y. Yang and D. L. Wang, *Chin. J. Catal.*, 2023, **55**, 116–136.

32 Y. Y. Liao, R. C. He, W. H. Pan, Y. Li, Y. Y. Wang, J. Li and Y. X. Li, *Chem. Eng. J.*, 2023, **464**, 142669.

33 Z. Xiao, C. Xie, Y. Wang, R. Chen and S. Wang, *J. Energy Chem.*, 2021, **53**, 208–225.

34 S. N. Fan, G. C. Yang, Y. Q. Jiao, Y. Liu, J. Q. Wang, H. J. Yan and H. G. Fu, *Adv. Mater.*, 2025, **37**, 2502523.

35 K. W. Bo, C. Z. Feng, S. S. Tang, Y. T. Wu, Q. J. Tao, Q. Lan, H. J. Zhang and Y. Wang, *Appl. Catal., B*, 2026, **385**, 126272.

36 S. J. Guan, Y. L. Cheng, L. Hao, H. Yoshida, C. Tarashima, T. Z. Zhan, T. Itoi, T. B. Qiu and Y. Lu, *Sci. Rep.*, 2023, **13**, 14105.

37 X. S. Kang, G. H. Dong and T. T. Dong, *ACS Appl. Energy Mater.*, 2023, **6**, 1025–1036.

38 J. W. Guo, H. B. Zhao, Z. W. Yang, L. W. Wang, A. Z. Wang, J. Zhang, L. H. Ding, L. F. Wang, H. Liu and X. Yu, *Adv. Funct. Mater.*, 2024, **34**, 2315714.

39 G. Gao, Y. T. Deng, X. K. Wang, J. Z. Wang, T. Li, C. Chen, Y. Q. Wang, Y. M. Li, M. M. Hu, G. C. Li, L. Wang, Z. J. Li, G. M. Zhou, J. Zhao and D. S. Wang, *Adv. Funct. Mater.*, 2025, **35**, 2508406.

40 Y. Zhao, B. Zhang, B. Xia, Z. Liu, C. Tan, C. Song, M. Fujii, L. Ma and M. Song, *ACS ES&T Eng.*, 2024, **4**, 2025–2035.

41 Q. B. Jiang, H. F. Xu, K. S. Hui, Y. J. Wei, L. W. Liu, Z. Q. Ye, C. Y. Zha, M. T. Zheng, J. Lu and K. N. Hui, *Adv. Mater.*, 2025, **37**, 2415986.

42 J. J. Yang, Z. Y. Cao, Y. J. Wan, S. H. Guan, B. Jiang, Y. Yamauchi and H. X. Li, *Adv. Energy Mater.*, 2025, **15**, 2404936.

43 W. J. He, R. Zhang, J. Y. Zhang, F. Q. Wang, Y. Li, J. L. Zhao, C. Chen, H. Liu and H. L. Xin, *J. Catal.*, 2022, **410**, 112–120.

44 Z. H. Yin, Y. M. Fan, K. P. Song, L. Chen, H. Tan, C. Q. Li, Y. P. Zhang, H. G. Zhang and J. J. Wang, *Adv. Funct. Mater.*, 2025, **36**, e12013.

45 Z. Y. Li, D. Wang, H. G. Kang, Z. N. Shi, X. W. Hu, H. B. Sun and J. L. Xu, *J. Mater. Chem. A*, 2024, **13**, 587–594.

46 Y. S. Lv, S. X. Bi, Z. M. Ma, Y. Shu, P. F. Zhang and Z. H. Luo, *ACS Catal.*, 2025, **15**, 19135–19147.

47 A. K. Rai, A. A. Shah, A. B. Dar, J. Kumar and M. Shrivastava, *Small Methods*, 2025, **9**, 2401001.

48 Z. Chen, N. Han, W. Wei, D. Chu and B.-J. Ni, *EcoEnergy*, 2024, **2**, 114–140.

49 Y.-N. Zhou, W.-L. Yu, H.-J. Liu, R.-Y. Fan, G.-Q. Han, B. Dong and Y.-M. Chai, *EcoEnergy*, 2023, **1**, 425–436.

50 Y. Qi, B. W. Liu, X. Q. Qiu, X. Z. Zeng, Z. C. Luo, W. D. Wu, Y. C. Liu, L. H. Chen, X. H. Zu, H. F. Dong, X. L. Lin and Y. L. Qin, *Adv. Mater.*, 2023, **35**, 2208284.

51 S. Dyjak, B. J. Jankiewicz, S. Kaniecki and W. Kicinski, *Green Chem.*, 2024, **26**, 2985–3020.

52 G. Wang, Y. Sun, Y. Zhao, C. Deng, Y. Zhu and Y. Li, *Nano Res.*, 2025, **18**, 94907165.

53 S. H. Wang, M. Li, H. L. Tang and H. N. Zhang, *Small*, 2025, **21**, 2411397.

54 Q. M. Peng, J. Q. Zhu, F. L. Wei, T. T. Isimjan, T. X. Sun, X. L. Yang, Y. F. Zhu and B. Wu, *Appl. Catal., B*, 2026, **384**, 126158.

55 X. W. Fu, X. C. Zang, J. X. Gao, H. D. Li, W. P. Xiao, Y. X. Zong, G. Y. Fu, J. S. Wang, T. Y. Ma, W. Jin, Z. X. Wu and L. Wang, *Adv. Energy Mater.*, 2025, **15**, 2501054.

56 F. Liu and Z. X. Fan, *Chem. Soc. Rev.*, 2023, **52**, 1723–1772.

57 K. Zhou, Y. S. Zhang, M. Y. Zhang, A. Rezayan, Z. Quan, D. D. Han, J. S. Wang, D. Wu and C. B. Xu, *Chem. Eng. J.*, 2024, **492**, 152347.

58 B. B. Liu, H. L. Liu, S. Z. Sun, Z. X. Ma, Y. X. Zhang, R. F. Nie and J. Fu, *Adv. Funct. Mater.*, 2025, **35**, 2504172.

59 Y. T. Li, C. R. Zhao, W. Wang, X. Wu and Y. D. Huang, *Mater. Chem. Front.*, 2025, **9**, 243–252.

60 S. D. Yang, X. Guo, X. N. Li, T. Z. Wu, L. H. Zou, Z. Y. He, Q. Xu, J. J. Zheng, L. Chen, Q. Y. Wang and Z. J. Xu, *Angew. Chem., Int. Ed.*, 2024, **63**, e202317957.

61 Z. Sofer, Y. Zuo, N. Antonatos, L. Dekanovsky, J. Luxa, J. D. Elliott, D. Gianolio, J. Saturala, F. Guzzetta, S. Mourdikoudis, J. Regner and R. Melek, *ACS Catal.*, 2023, **13**, 2601–2609.

62 J. L. Zhu, J. M. Qian, X. B. Peng, B. R. Xia and D. Q. Gao, *Nano-Micro Lett.*, 2023, **15**, 30.

63 L. S. Peng, N. Yang, Y. Q. Yang, Q. Wang, X. Y. Xie, D. Sun-Waterhouse, L. Shang, T. R. Zhang and G. I. N. Waterhouse, *Angew. Chem., Int. Ed.*, 2021, **60**, 24612–24619.

64 Y. Zhou, D. F. Yan, Q. F. Gu, S. H. Zhu, L. Wang, H. G. Peng and Y. Zhao, *Appl. Catal., B*, 2021, **285**, 119792.

65 J. Jin, X. Han, Y. Y. Fang, Z. D. Zhang, Y. P. Li, T. Y. Zhang, A. J. Han and J. F. Liu, *Adv. Funct. Mater.*, 2022, **32**, 2109218.

66 P. L. Zhai, M. Y. Xia, Y. Z. Wu, G. H. Zhang, J. F. Gao, B. Zhang, S. Y. Cao, Y. T. Zhang, Z. W. Li, Z. Z. Fan, C. Wang, X. M. Zhang, J. T. Miller, L. C. Sun and J. G. Hou, *Nat. Commun.*, 2021, **12**, 4587.

67 P. Zhou, Y. Y. Wang, C. Xie, C. Chen, H. W. Liu, R. Chen, J. Huo and S. Y. Wang, *Chem. Commun.*, 2017, **53**, 11778–11781.

68 L. Li, Z. D. Qin, L. Ries, S. Hong, T. Michel, J. Yang, C. Salameh, M. Bechelany, P. Miele, D. Kaplan, M. Chhowalla and D. Voiry, *ACS Nano*, 2019, **13**, 6824–6834.

69 M. M. Yan, Z. X. Wei, Z. C. Gong, B. Johannessen, G. L. Ye, G. C. He, J. J. Liu, S. L. Zhao, C. Y. Cui and H. L. Fei, *Nat. Commun.*, 2023, **14**, 368.

70 K. Huang, Z. X. Wei, J. B. Liu, Z. C. Gong, J. J. Liu, M. N. Yan, G. C. He, H. S. Gong, Y. F. Hu, Y. M. He, S. L. Zhao, G. L. Ye and H. L. Fei, *Small*, 2022, **18**, 2201139.

71 Q. C. Wang, Q. G. Feng, Y. P. Lei, S. H. Tang, L. Xu, Y. Xiong, G. Z. Fang, Y. C. Wang, P. Y. Yang, J. J. Liu, W. Liu and X. Xiong, *Nat. Commun.*, 2022, **13**, 3689.

72 X. Zhang, Y. Jiang, T. Wang, C. Wang, D. Wang, Y. Qiu and Y. Zhang, *Mater. Futures*, 2025, **5**, 015103.

73 J. J. Liu, Z. X. Wei, Z. C. Gong, M. M. Yan, Y. F. Hu, S. L. Zhao, G. L. Ye and H. L. Fei, *Appl. Catal., B*, 2023, **324**, 122267.

74 H. Ma, W. S. Yan, Y. L. Yu, L. H. Deng, Z. Hong, L. Song and L. Li, *Nanoscale*, 2023, **15**, 1357–1364.

75 X. Zhou, M. K. Ke, G. X. Huang, C. Chen, W. X. Chen, K. Liang, Y. T. Qu, J. Yang, Y. Wang, F. T. Li, H. Q. Yu and Y. E. Wu, *Proc. Natl. Acad. Sci. U. S. A.*, 2022, **119**, e2119492119.

76 Z. Liu, X. X. Wang, R. Guo, J. J. Richardson, T. Z. Wang, W. J. Xu, F. Caruso and S. J. Pan, *Adv. Funct. Mater.*, 2023, **33**, 2211563.

77 P. Shen, X. C. Li, Y. J. Luo, Y. L. Guo, X. L. Zhao and K. Chu, *ACS Nano*, 2022, **16**, 7915–7925.

78 H. L. Fei, J. C. Dong, Y. X. Feng, C. S. Allen, C. Z. Wan, B. Volosskiy, M. F. Li, Z. P. Zhao, Y. L. Wang, H. T. Sun, P. F. An, W. X. Chen, Z. Y. Guo, C. Lee, D. L. Chen, I. Shakir, M. J. Liu, T. D. Hu, Y. D. Li, A. I. Kirkland, X. F. Duan and Y. Huang, *Nat. Catal.*, 2018, **1**, 63–72.

79 Y. Q. Zhang, L. Tao, C. Xie, D. D. Wang, Y. Q. Zou, R. Chen, Y. Y. Wang, C. K. Jia and S. Y. Wang, *Adv. Mater.*, 2020, **32**, 1905923.

80 Q. Wang, H. Xu, X. Y. Qian, G. Y. He and H. Q. Chen, *Appl. Catal., B*, 2023, **322**, 122104.

81 L. M. Wang, L. L. Zhang, W. Ma, H. Wan, X. J. Zhang, X. Zhang, S. Y. Jiang, J. Y. Zheng and Z. Zhou, *Adv. Funct. Mater.*, 2022, **32**, 2203342.

82 H. W. Zhao, S. L. Zhu, Z. D. Cui, Z. Y. Li, S. L. Wu, W. C. Xu, Z. H. Gao, Y. Q. Liang, L. L. Ma and H. Jiang, *Adv. Funct. Mater.*, 2025, **35**, 2423549.

83 Y. Q. Zhang, J. J. Liu, Y. F. Xu, C. Xie, S. Y. Wang and X. D. Yao, *Chem. Soc. Rev.*, 2024, **53**, 10620–10659.

84 H. Z. Yu, M. Y. Hu, C. Chen, C. J. Hu, Q. H. Li, F. Hu, S. J. Peng and J. Ma, *Angew. Chem., Int. Ed.*, 2023, **62**, e202314569.

85 M. Boutonnet Kizling and S. G. Järås, *Appl. Catal., A*, 1996, **147**, 1–21.

86 W. Chu, L. N. Wang, P. A. Chernavskii and A. Y. Khodakov, *Angew. Chem., Int. Ed.*, 2008, **47**, 5052–5055.

87 Z. Wang, Y. Zhang, E. C. Neyts, X. X. Cao, X. S. Zhang, B. W. L. Jang and C. J. Liu, *ACS Catal.*, 2018, **8**, 2093–2110.

88 Y. Y. Wang, Y. Q. Zhang, Z. J. Liu, C. Xie, S. Feng, D. D. Liu, M. F. Shao and S. Y. Wang, *Angew. Chem., Int. Ed.*, 2017, **56**, 5867–5871.

89 F. Q. Wang, Y. Y. Zhang, W. H. Yuan, J. Mao, K. Wang, Y. Li, C. Chen, L. M. Liang and C. C. Liu, *ACS Appl. Nano Mater.*, 2023, **6**, 3848–3855.

90 G. L. Ye, Y. J. Gong, J. H. Lin, B. Li, Y. M. He, S. T. Pantelides, W. Zhou, R. Vajtai and P. M. Ajayan, *Nano Lett.*, 2016, **16**, 1097–1103.

91 Z. J. Xu, J. L. Wu, W. H. Chen, Z. Q. Jiang, J. Cao, G. L. Chen and Z. J. Jiang, *Adv. Funct. Mater.*, 2025, **35**, e11117.

92 C.-J. Liu, J. Zou, K. Yu, D. Cheng, Y. Han, J. Zhan, C. Ratanatawanate and B. W. L. Jang, *Pure Appl. Chem.*, 2006, **78**, 1227–1238.

93 X. R. Zhuge, C. F. Wang, Y. H. Li, Y. X. Zong, W. P. Xiao, D. H. Chen, J. S. Wang, T. Y. Ma, M. Song, Z. X. Wu and L. Wang, *Sci. China Mater.*, 2025, **68**, 4471–4480.

94 E. Z. Li, Y. Z. Shen, Y. H. Li, Y. X. Zong, W. P. Xiao, G. R. Xu, J. S. Wang, H. Li, T. Y. Ma, Z. X. Wu and L. Wang, *Appl. Catal., B*, 2026, **382**, 126022.

95 C. Gabriel, S. Gabriel, E. H. Grant, E. H. Grant, B. S. J. Halstead and D. M. P. Mingos, *Chem. Soc. Rev.*, 1998, **27**, 213–224.

96 J. Huang, X. Xu, Y. Yan, Y. Zheng, Y. Yao, Z. Li, Y. Yan, K. N. Hui, J. Zou and M. Liu, *Adv. Energy Mater.*, 2025, **15**, 2500360.

97 Y. H. Zhang, S. Wu, T. Sun, Q. G. Li and G. Y. Fan, *J. Colloid Interface Sci.*, 2025, **681**, 71–81.

98 M. A. Khan, M. S. Akhtar and O.-B. Yang, *Sol. Energy*, 2010, **84**, 2195–2201.

99 D. S. Zhang, B. Goekce and S. Barcikowski, *Chem. Rev.*, 2017, **117**, 3990–4103.

100 R. Q. Ye, D. K. James and J. M. Tour, *Acc. Chem. Res.*, 2018, **51**, 1609–1620.

101 B. Wang, X. Zhu, X. D. Pei, W. G. Liu, Y. C. Leng, X. W. Yu, C. Wang, L. H. Hu, Q. M. Su, C. P. Wu, Y. F. Yao, Z. Q. Lin and Z. G. Zou, *J. Am. Chem. Soc.*, 2023, **145**, 13788–13795.

102 W. D. Yi, H. Q. Jiang and G. J. Cheng, *Small*, 2022, **18**, 2202403.

103 S. Y. Liu and C. R. Liu, *Cryst. Growth Des.*, 2019, **19**, 2912–2918.

104 W. H. Guo, Y. F. Zhang, J. J. Su, Y. Song, L. B. Huang, L. Cheng, X. H. Cao, Y. B. Dou, Y. B. Ma, C. Y. Ma, H. Zhu, T. T. Zheng, Z. Y. Wang, H. Li, Z. X. Fan, Q. Liu, Z. Y. Zeng, J. C. Dong, C. A. Xia, B. Z. Tang and R. Q. Ye, *Small*, 2022, **18**, 2201311.

105 Z. H. Xiao, X. B. Huang, L. Xu, D. F. Yan, J. Huo and S. Y. Wang, *Chem. Commun.*, 2016, **52**, 13008–13011.

106 X. L. Fan, D. W. Chang, X. L. Chen, J. B. Baek and L. M. Dai, *Curr. Opin. Chem. Eng.*, 2016, **11**, 52–58.

107 I. Y. Jeon, S. Y. Bae, J. M. Seo and J. B. Baek, *Adv. Funct. Mater.*, 2015, **25**, 6961–6975.

108 X. S. Qiao, H. J. Kang, Y. Li, K. Cui, X. Jia, X. H. Wu and W. Qin, *Appl. Catal., B*, 2022, **305**, 121034.

109 Y. Zhao, B. Zhang, B. Xia, Z. Liu, C. Tan, C. Song, M. Fujii, L. Ma and M. Song, *ACS ES&T Eng.*, 2024, **4**, 2025–2035.

110 A. P. Amrute, J. De Bellis, M. Felderhoff and F. Schüth, *Chem.–Eur. J.*, 2021, **27**, 6819–6847.

111 E. L. Lawrence, B. D. A. Levin, T. Boland, S. L. Y. Chang and P. A. Crozier, *ACS Nano*, 2021, **15**, 2624–2634.

112 C. Zhang, B. H. Chen, D. H. Mei and X. Liang, *J. Mater. Chem. A*, 2019, **7**, 5475–5481.

113 X. H. Sun, D. X. Wu, W. H. Zhu, X. B. Chen, R. Sharma, J. C. Yang and G. W. Zhou, *J. Phys. Chem. Lett.*, 2021, **12**, 9547–9556.

114 F. Esch, S. Fabris, L. Zhou, T. Montini, C. Africh, P. Fornasiero, G. Comelli and R. Rosei, *Science*, 2005, **309**, 752–755.

115 F. X. Zhang, B. Y. Li, X. Quan, K. Wang, J. Y. Xu, T. T. Wu, Z. L. Li, M. Yan, S. J. Liu, Y. He, Y. Shi, Y. Q. Su and P. F. Xie, *ACS Catal.*, 2024, **14**, 7136–7148.

116 Z. X. Li, H. C. Yang, C. W. Zhong, S. W. Deng and E. Z. Li, *Acta Mater.*, 2026, **303**, 121740.

117 J. G. Lin, F. Liu, W. Q. Cheng, Y. Ma, G. Xue, S. L. Liang, Y. C. Wang, P. Y. Cao, Y. Zhang and X. L. Wu, *Acta Mater.*, 2026, **303**, 121730.

118 M. Setvin, M. Schmid and U. Diebold, *Phys. Rev. B*, 2015, **91**, 195403.

119 L. P. Bao, S. Ali, C. H. Dai, Q. Zeng, C. Zeng, Y. S. Jia, X. Liu, P. Wang, X. H. Ren, T. Yang, M. Bououdina, Z. H. Lu, Y. C. Wei, X. Yu and Y. T. Zhou, *ACS Nano*, 2024, **18**, 5878–5889.

120 H. J. Li, K. Xi, W. Wang, S. Liu, G. R. Li and X. P. Gao, *Energy Storage Mater.*, 2022, **45**, 1229–1237.

121 D. Q. Wang, Y. Zhang, C. Zhao, Z. Q. Li, R. L. Qiu, Q. L. Shuai, H. Q. Wang and Q. S. Hua, *ACS Appl. Mater. Interfaces*, 2025, **17**, 45687–45695.

122 M. Harrison, D. Woodruff, J. Robinson, D. Sander, W. Pan and J. Kirschner, *Phys. Rev. B: Condens. Matter Mater. Phys.*, 2006, **74**, 165402.

123 Y. Grunder, C. A. Lucas, P. B. Thompson, Y. Joly and Y. Soldo-Olivier, *J. Phys. Chem. C*, 2022, **126**, 4612–4619.

124 X. H. Sun, W. H. Zhu, D. X. Wu, C. R. Li, J. Y. Wang, Y. G. Zhu, X. B. Chen, J. A. Boscoboinik, R. Sharma and G. W. Zhou, *Nat. Commun.*, 2020, **11**, 305.

125 Q. Hu, Y. J. Qin, X. D. Wang, Z. Y. Wang, X. W. Huang, H. J. Zheng, K. R. Gao, H. P. Yang, P. X. Zhang, M. H. Shao and C. X. He, *Energy Environ. Sci.*, 2021, **14**, 4989–4997.

126 C. Yang, C. S. Chen, T. Y. Bian, C. Xu, X. L. Che, D. Y. Li, K. Liang, X. Z. Dong, J. Yin, G. Li and Y. Zhu, *ACS Nano*, 2025, **19**, 9225–9231.

127 J. L. Qi, T. X. Xu, J. Cao, S. Guo, Z. X. Zhong and J. C. Feng, *Nanoscale*, 2020, **12**, 6204–6210.

128 C. L. Zhang, G. J. Liu, P. Wu, G. F. Zeng and Y. H. Sun, *Chemcatchem*, 2020, **12**, 3512–3522.

129 J. R. Han, H. B. Wang, Y. T. Wang, H. Zhang, J. Li, Y. J. Xia, J. S. Zhou, Z. Y. Wang, M. C. Luo, Y. H. Wang, N. Wang, E. Cortes, Z. M. Wang, A. Vomiero, Z. F. Huang, H. X. Ren, X. M. Yuan, S. H. Chen, D. H. Feng, X. H. Sun, Y. C. Liu and H. Y. Liang, *Angew. Chem., Int. Ed.*, 2024, **63**, e202405839.

130 S. Li, H. Yang, H. Tong, W. Xu, Z. Wang, W. Lu, X. Deng and L. Li, *Adv. Mater.*, 2025, **37**, e11910.

131 Y. Zou, X. Li, Y. Zhao, X. Liu, S. Xie, F. Liu and T. Zhu, *ACS Catal.*, 2025, **15**, 6346–6360.

132 Y. Li, Z. Zhang, R. Wei, X. Zhang, R. Geng, F. Zheng, L. Wang, Y. Wang and S. Yin, *Chem. Eng. J.*, 2025, **527**, 171700.

133 H. Arandiyan, S. S. Mofarah, C. C. Sorrell, E. Doustkhah, B. Sajjadi, D. Hao, Y. Wang, H. Sun, B.-J. Ni, M. Rezaei, Z. Shao and T. Maschmeyer, *Chem. Soc. Rev.*, 2021, **50**, 10116–10211.

134 Z. J. Chen, Q. Shao, J. Wu, J. Zheng, S. Bao, L. Zhang, T. Zhang, X. Lan, Y. Sun and D. Wang, *Angew. Chem., Int. Ed.*, 2025, **64**, e202500678.

135 Y. Wang, T. Wang, H. Arandiyan, G. Song, H. Sun, Y. Sabri, C. Zhao, Z. Shao and S. Kawi, *Adv. Mater.*, 2024, **36**, 2313378.

136 K. Y. Zhu, X. F. Zhu and W. S. Yang, *Angew. Chem., Int. Ed.*, 2019, **58**, 1252–1265.

137 Y. Jia, L. Z. Zhang, L. Z. Zhuang, H. L. Liu, X. C. Yan, X. Wang, J. D. Liu, J. C. Wang, Y. R. Zheng, Z. H. Xiao, E. Taran, J. Chen, D. J. Yang, Z. H. Zhu, S. Y. Wang, L. M. Dai and X. D. Yao, *Nat. Catal.*, 2019, **2**, 688–695.

138 T. C. Liu, L. P. Lin, X. X. Bi, L. L. Tian, K. Yang, J. J. Liu, M. F. Li, Z. H. Chen, J. Lu, K. Amine, K. Xu and F. Pan, *Nat. Nanotechnol.*, 2019, **14**, 50–56.

139 R. G. Mariano, M. Kang, O. J. Wahab, I. J. McPherson, J. A. Rabinowitz, P. R. Unwin and M. W. Kanan, *Nat. Mater.*, 2021, **20**, 1000–1006.

140 Y. Zhao, S. Gao, X. Y. Chen, Y. Liu, M. J. Zhang, Y. F. Liu, J. X. Kang, T. Q. Guo, L. M. Liu and L. Guo, *J. Am. Chem. Soc.*, 2025, **147**, 31722–31730.

141 S. A. Bonke, T. Risse, A. Schnegg and A. Brückner, *Nat. Rev. Methods Primers*, 2021, **1**, 33.

142 A. Brückner, *Chem. Soc. Rev.*, 2010, **39**, 4673–4684.

143 J. Fischer, M. Agrachev, J. Forrer, R. Tschaggelar, O. Oberhänsli and G. Jeschke, *Chimia*, 2024, **78**, 326–332.

144 T. P. Araújo, J. Morales-Vidal, T. S. Zou, M. Agrachev, S. Verstraeten, P. O. Willi, R. N. Grass, G. Jeschke, S. Mitchell, N. López and J. Pérez-Ramírez, *Adv. Energy Mater.*, 2023, **13**, 2204122.

145 T. Pinheiro Araújo, C. Mondelli, M. Agrachev, T. Zou, P. O. Willi, K. M. Engel, R. N. Grass, W. J. Stark, O. V. Safonova and G. Jeschke, *Nat. Commun.*, 2022, **13**, 5610.

146 F. Z. Sun, Z. Li, H. Xu, Y. Fu, H. Li, Y. Y. Yao, L. Ren, X. Q. He, Y. H. Li, R. Yang, N. Zhang, Z. G. Hu, T. Y. Ma and J. X. Zou, *Adv. Energy Mater.*, 2024, **14**, 2400875.

147 H. Z. Yang, N. Guo, S. B. Xi, H. Y. Zou, J. Y. Chen, L. Fan, Y. K. Xiao, Q. He, L. L. Duan, P. F. Wei, G. X. Wang, C. Zhang and L. Wang, *Adv. Mater.*, 2025, **37**, 2510192.

148 P. P. Zhang, Y. R. Yu, K. Z. Li, R. L. Yang, R. H. Hou, Y. K. Li, Y. X. Wei, M. Cai, G. S. Shao and P. Zhang, *Adv. Energy Mater.*, 2025, **16**, 2501940.

149 Z. H. Xiao, Y. C. Huang, C. L. Dong, C. Xie, Z. J. Liu, S. Q. Du, W. Chen, D. F. Yan, L. Tao, Z. W. Shu, G. H. Zhang, H. G. Duan, Y. Y. Wang, Y. Q. Zou, R. Chen and S. Y. Wang, *J. Am. Chem. Soc.*, 2020, **142**, 12087–12095.

150 L. Z. Sun, X. Pan, Y. N. Xie, J. G. Zheng, S. H. Xu, L. Li and G. H. Zhao, *Angew. Chem., Int. Ed.*, 2024, **63**, e202402176.

151 A. C. Ferrari and D. M. Basko, *Nat. Nanotechnol.*, 2013, **8**, 235–246.

152 F. Y. Hu, R. P. Ye, C. K. Jin, D. Liu, X. H. Chen, C. Li, K. H. Lim, G. Q. Song, T. C. Wang, G. Feng, R. B. Zhang and S. Kawi, *Appl. Catal., B*, 2022, **317**, 121715.

153 T. L. Hou, J. X. Zhu, H. F. Gu, X. Y. Li, Y. Q. Sun, Z. Hua, R. W. Shao, C. Chen, B. T. Hu, L. Q. Mai, S. H. Chen, D. S. Wang and J. T. Zhang, *Angew. Chem., Int. Ed.*, 2025, **64**, e202424749.

154 Y. J. Wu, J. Yang, T. X. Tu, W. Q. Li, P. F. Zhang, Y. Zhou, J. F. Li, J. T. Li and S. G. Sun, *Angew. Chem., Int. Ed.*, 2021, **60**, 26829–26836.

155 X. W. Wang, Y. Y. Zhang, S. Wang, Y. F. Li, Y. F. Feng, Z. C. Dai, Y. X. Chen, X. M. Meng, J. Xia and G. Q. Zhang, *Angew. Chem., Int. Ed.*, 2024, **63**, e202407665.

156 M. S. A. Sher Shah, G. Y. Jang, K. Zhang and J. H. Park, *EcoEnergy*, 2023, **1**, 344–374.

157 X. Wang, H. Zhao, H. Li, W. Xiao, G. Xu, G. Fu, L. Wang and Z. Wu, *Inorg. Chem. Front.*, 2025, **12**, 8118–8127.

158 X. Liu, R. Y. Liu, J. X. Qiu, X. Cheng and G. G. Li, *Angew. Chem., Int. Ed.*, 2020, **132**, 14066–14071.

159 Y. J. Pan, Z. C. Wang, K. X. Wang, Q. Ye, B. S. Shen, F. S. Yang and Y. L. Cheng, *Adv. Funct. Mater.*, 2024, **34**, 2402264.

160 J. X. Zhao, K. J. Wang, X. Y. Li, X. M. Li, X. Y. Cui and X. Zhao, *Angew. Chem., Int. Ed.*, 2025, **64**, e202513592.

161 S. W. Ding, Z. H. Li, G. X. Lin, Y. X. Ding, L. Q. Wang and L. C. Sun, *Angew. Chem., Int. Ed.*, 2025, **64**, e202517132.

162 H. J. Niu, N. Ran, W. Zhou, W. X. An, C. X. Huang, W. X. Chen, M. Zhou, W. F. Lin, J. J. Liu and L. Guo, *J. Am. Chem. Soc.*, 2025, **147**, 2607–2615.

163 S. Qi, J. You, X. Y. Liufu, Y. Zhang, R. B. Chen, J. P. Zhuang, T. Y. Liang, L. L. Li, Q. H. Huo, C. Y. Shang, X. Zhang, H. P. Yang, Q. Hu and C. X. He, *Adv. Mater.*, 2025, **38**, e12188.

164 T. Guo, P. Hu, L. Li, Z. Wang and L. Guo, *Chem*, 2023, **9**, 1080–1093.

165 B. Zhou, J. Zhou, L. Wang, J. H. Kang, A. Zhang, J. Zhou, D. Zhang, D. Xu, B. Hu and S. Deng, *Nat. Synth.*, 2024, **3**, 67–75.

166 B. X. Shen, S. Li, M. T. Yang, K. Ge, H. J. Xia, Q. Y. Li, F. Ge and Y. D. Hu, *ACS Appl. Mater. Interfaces*, 2025, **17**, 29628–29638.

167 X. M. Li, B. Han, R. X. Zhu, R. C. Shi, M. Wu, Y. W. Sun, Y. H. Li, B. Y. Liu, L. F. Wang, J. M. Zhang, C. B. Tan, P. Gao and X. D. Bai, *Proc. Natl. Acad. Sci. U. S. A.*, 2023, **120**, e2213650120.

168 J. Wu, X. H. Gao and Z. W. Chen, *Chem. Eng. J.*, 2024, **492**, 152241.

169 S. Tao, G. K. Zhang, B. Qian, J. Yang, S. Q. Chu, C. C. Sun, D. J. Wu, W. S. Chu and L. Song, *Appl. Catal., B*, 2023, **330**, 122600.

170 Z. M. Li, J. H. Yi, Y. Tang, Z. F. Zhang, C. P. Li, R. Bao and J. S. Wang, *Energy Environ. Sci.*, 2025, **18**, 7188–7202.

171 J. J. Zhang, L. L. Xu, X. X. Yang, S. Guo, Y. F. Zhang, Y. Zhao, G. Wu and G. Li, *Angew. Chem., Int. Ed.*, 2024, **63**, e202405641.

172 Y. C. Lin, Z. Q. Tian, L. J. Zhang, J. Y. Ma, Z. Jiang, B. J. Deibert, R. X. Ge and L. Chen, *Nat. Commun.*, 2019, **10**, 162.

173 R. X. Ge, L. Li, J. W. Su, Y. C. Lin, Z. Q. Tian and L. Chen, *Adv. Energy Mater.*, 2019, **9**, 1901313.

174 J. W. Tao, R. Q. Gao, G. Y. Lin, C. Y. Chu, Y. Sun, C. Y. Yu, Y. H. Ma and H. B. Qiu, *Nat. Commun.*, 2025, **16**, 4996.

175 S.-Y. Yuan, T.-T. Li, J.-Y. Cui, J.-K. Sun, Y.-S. Gong, A. Braun, H. Liu and J.-J. Wang, *EcoEnergy*, 2024, **2**, 322–335.

176 H. F. Wang, C. Lin, L. Tan, J. Shen, X. T. Wu, X. X. Pan, Y. H. Zhao, H. J. Zhang, Y. Sun, B. B. Mei, H. D. Um, Q. Xiao, W. Jiang, X. P. Li and W. Luo, *Nat. Commun.*, 2025, **16**, 3976.

177 M. Jin, J. Chen, X. Han, Y. Guo, Y. Liu, J. Wang, J. Li, Y. Yuan, H. Jin, S. Wang and X. Huang, *Nat. Commun.*, 2025, **16**, 11615.

178 N. Zhang, X. Y. Liu, H. X. Zhong, W. Liu, D. Bao, J. R. Zeng, D. P. Wang, C. N. Ma and X. B. Zhang, *Angew. Chem., Int. Ed.*, 2025, **64**, e202503246.

179 J. Yang, K. Y. An, Z. C. Yu, L. L. Qiao, Y. P. Cao, Y. J. Zhuang, C. F. Liu, L. Li, L. S. Peng and H. Pan, *ACS Catal.*, 2024, **14**, 17739–17747.

180 H. Liu, Y. Zhang, Z. Y. Liu, S. C. Wang, X. Q. Mu, Q. H. Zhang, W. Cao, S. L. Liu, D. S. Wang and Z. H. Dai, *J. Am. Chem. Soc.*, 2025, **147**, 44141–44151.

181 S. X. Li, S. Zhao, S. F. Hung, L. M. Deng, L. Q. Wang, F. K. Shi, A. Dong, Y. Zhang, T. Y. Chen, F. Hu, L. L. Li, S. Ramakrishna, Y. P. Wu and S. J. Peng, *J. Am. Chem. Soc.*, 2025, **147**, 33770–33779.

182 J. Han, M. K. Nam, S. Shin, I. Cho, H. Jeon, J. Heo, J. Lee, M. K. Cho, D. J. Preston, M. C. Hersam, I. S. Kim, B. Shong and W. K. Lee, *J. Am. Chem. Soc.*, 2025, **147**, 41096–41108.

183 Z. X. Wu, Y. L. Wang, D. Z. Liu, B. W. Zhou, P. F. Yang, R. Z. Liu, W. P. Xiao, T. Y. Ma, J. S. Wang and L. Wang, *Adv. Funct. Mater.*, 2023, **33**, 2307010.

184 Y. Liu, Y. Huang, D. J. Wu, H. Jang, J. H. Wu, H. R. Li, W. X. Li, F. Zhu, M. G. Kim, D. L. Zhou, X. K. Xi, Z. W. Lei, Y. C. Zhang, Y. Deng, W. S. Yan, M. D. Gu, J. Jiang, S. H. Jiao and R. G. Cao, *J. Am. Chem. Soc.*, 2024, **146**, 26897–26908.

185 Y. Ou, L. Liu, X. Peng, L. Zhang, Z. Ou, W. Zhang and Y. Zhang, *Nano Mater. Sci.*, 2024, **6**, 565–575.

186 X. W. Guo, E. H. Song, W. Zhao, S. M. Xu, W. L. Zhao, Y. J. Lei, Y. Q. Fang, J. J. Liu and F. Q. Huang, *Nat. Commun.*, 2022, **13**, 5954.

187 W. Q. Zhan, X. W. Zhai, Y. H. Li, M. Wang, H. Wang, L. Wu, X. F. Tang, H. J. Zhang, B. J. Ye, K. B. Tang, G. M. Wang and M. Zhou, *ACS Nano*, 2024, **18**, 10312–10323.

188 G. H. Zhang, S. L. Qi, H. D. Wang, X. F. Lei, Z. X. Zhang, W. Liu, X. Y. Liu, Y. Zhao, L. Yang, W. G. Ma, W. J. Fan and X. Zong, *Adv. Funct. Mater.*, 2025, e17113.

189 H. Zhang, A. R. Chen, Z. H. Bi, X. Z. Wang, X. J. Liu, Q. Q. Kong, W. Zhang, L. Q. Mai and G. Z. Hu, *ACS Nano*, 2023, **17**, 24070–24079.

190 H. Y. Wang, S. X. Zhai, H. Wang, F. X. Yan, J. T. Ren, L. Wang, M. L. Sun and Z. Y. Yuan, *ACS Nano*, 2024, **18**, 19682–19693.

191 L. Wang, X. W. Lv, H. Y. Wang, J. T. Ren, Y. Feng, M. L. Sun and Z. Y. Yuan, *Adv. Energy Mater.*, 2025, **15**, e04036.

192 Z. Zhao, J. P. Sun, X. Li, S. Y. Qin, C. H. Li, Z. S. Zhang, Z. Z. Li and X. C. Meng, *Nat. Commun.*, 2024, **15**, 7475.

193 Y. M. Zhang, L. L. Zhao, J. Wang, Y. Liu, Z. D. Zhang, W. W. Cai, J. Z. Ma and J. T. Zhang, *J. Am. Chem. Soc.*, 2025, **147**, 27367–27376.

194 Y. Yao, E. L. Hu, Z. Y. Wang, Y. J. Cui and G. D. Qian, *ACS Omega*, 2022, **7**, 2244–2251.

195 C. A. Zhou, K. Ma, Z. C. Zhuang, M. L. Ran, G. Q. Shu, C. Wang, L. Song, L. R. Zheng, H. R. Yue and D. S. Wang, *J. Am. Chem. Soc.*, 2024, **146**, 21453–21465.

196 Q. Wang, S.-F. Hung, K. Lao, X. Huang, F. Li, H. B. Tao, H. B. Yang, W. Liu, W. Wang and Y. Cheng, *Nat. Catal.*, 2025, **8**, 1–11.

197 C. Xu, H. Yu, H. Huang, S. Li, Y. Cao, W. Peng, Y. Li, H. Ke, S. Xu, H. Mo, C. Wu, H. Wang, Y. Zhang and X. Li, *Angew. Chem., Int. Ed.*, 2025, **64**, e202504667.

198 L. Wang, B. Li, M. Li, Y. Zhang, T. Yuan, Y. Ding, T. Li, C. Peng, S. Jiang and X. Xiong, *J. Am. Chem. Soc.*, 2025, **148**, 3128–3138.

199 Y. Q. Yang, D. W. Pang, C. J. Wang, Z. H. Fu, N. Y. Liu, J. J. Liu, H. J. Wu, B. B. Jia, Z. L. Guo, X. Y. Fan and J. L. Zheng, *Angew. Chem., Int. Ed.*, 2025, **64**, e202504084.

200 J. Li, Q. Wang, R. Guo, Y. Zong, J. Xing, W. Xiao, G. Xu, D. Chen, L. Wang and Z. Wu, *Inorg. Chem. Front.*, 2025, **12**, 5063–5072.

201 Y. H. He, X. P. Chen, Y. C. Lei, Y. Q. Liu and L. L. Wang, *Nanomaterials*, 2023, **13**, 2522.

202 N. N. Zhang, S. Y. Sun, C. Q. Cheng, F. F. Zhang, S. W. Yan, Z. L. Zhang, L. Q. Liu, Y. X. Li, L. Shang, R. Zhang, P. F. Yin, J. Yang, C. K. Dong, X. W. Du and H. Liu, *ACS Energy Lett.*, 2025, **10**, 5596–5604.

203 J. Ni, Z. P. Shi, Y. B. Wang, J. H. Yang, H. X. Wu, P. B. Wang, M. L. Xiao, C. P. Liu and W. Xing, *eScience*, 2025, **5**, 100295.

204 C. Tsai, H. Li, S. Park, J. Park, H. S. Han, J. K. Norskov, X. L. Zheng and F. Abild-Pedersen, *Nat. Commun.*, 2017, **8**, 15113.

205 Y. X. Zhao, M. T. Tang, S. D. Wu, J. Geng, Z. J. Han, K. Chan, P. Q. Gao and H. Li, *J. Catal.*, 2020, **382**, 320–328.

206 H. G. Han, J. W. Choi, M. Son and K. C. Kim, *eScience*, 2024, **4**, 100204.

207 J. Liu, J. Sun, X. Wang, Y. Wang, M. Li, M. Li, X. Zhang, H. Xia, J. Sun, D. Li and L. Zhang, *EcoEnergy*, 2025, **3**, e70021.

208 Q. Shi, P. Wang, M. Niu, Y. Zhang, H. Wang, J. Zhang, Y. Yamauchi, Y.-Z. Long and J. Zheng, *EcoEnergy*, 2026, **4**, e70029.

209 H. Meskher, A. R. Woldu, P. K. Chu, F. Lu and L. Hu, *EcoEnergy*, 2024, **2**, 630–651.

210 Y. Gu, Y. Zhang, X. Song, Y. Wang, A. Bao, D. Zhang, J. Lv, Z. Zheng, X. Zhang, Z. Liu and X. Qi, *Nano Res. Energy*, 2025, **4**, e9120189.

211 M. Song, X. Yang, C. Guo, S. Zhang, J. Ma and H. Gao, *EcoEnergy*, 2025, **3**, 470–481.

212 Z. Li, Y. Yao, S. Sun, J. Liang, S. Hong, H. Zhang, C. Yang, X. Zhang, Z. Cai and J. Li, *Angew. Chem., Int. Ed.*, 2024, **63**, e202316522.

213 H. Chen, Y.-Q. Wang, R. Ding, Z.-W. Zeng, B.-W. Liu, F.-R. Zeng, Y.-Z. Wang and H.-B. Zhao, *Matter*, 2024, **7**, 3189–3204.

214 P. Wang, P. Wang, T. Wu, X. Sun and Y. Zhang, *Adv. Sci.*, 2024, **11**, 2407892.

215 J. Hu, X. Tang, Q. Dai, Z. Liu, H. Zhang, A. Zheng, Z. Yuan and X. Li, *Nat. Commun.*, 2021, **12**, 3409.

216 H. Tang, J. Ding, Z. Feng, K. Shen, L. Chen and Y. Li, *Adv. Funct. Mater.*, 2025, e28467.

217 X. Wang, H. Hu, J. Song, J. Ma, H. Du, J. J. Wang, M. Wang, W. Chen, Y. Zhou and J. Wang, *Adv. Energy Mater.*, 2025, **15**, 2402883.

218 H. Mao, X. Liu, T. Cui, J. Tang, Z. Su, J. Chi, Y. Chai, Z. Wu and L. Wang, *Angew. Chem., Int. Ed.*, 2025, **64**, e202511867.

219 J. Duan, X. Zhao, Z. Luo, H. Sun, M. Chen, Q. Lu, B. Wang, B. Xiao, T. Zhou, D. Li, H. Cui, T. He and Q. Liu, *Appl. Catal., B*, 2025, **385**, 126271.

220 X. Fu, H. Li, Y. Zong, W. Xiao, J. Wang, H. Li, T. Ma, Z. Wu and L. Wang, *Angew. Chem., Int. Ed.*, 2025, **64**, e202512710.